The Sequence of Heavy Precipitation and Flash Flooding of 12 and 13 September 2019 in Eastern Spain. Part I: Mesoscale Diagnostic and Sensitivity Analysis of Precipitation

ALEJANDRO HERMOSO,[a] VICTOR HOMAR,[a] AND ARNAU AMENGUAL[a]

[a] Meteorology Group, Physics Department, Universitat de les Illes Balears, Palma, Mallorca, Spain

ABSTRACT: The Mediterranean region is frequently affected by heavy precipitation episodes and subsequent flash flooding. An exemplary case is the heavy precipitation episode that occurred in the regions of València, Murcia, and Almería (eastern Spain) on 12 and 13 September 2019. Observed rainfall amounts were close to 500 mm in 48 h, causing seven fatalities and estimated economical losses above EUR 425 million. This case exemplifies the challenging aspects of convective-scale forecasting in the Mediterranean region, with kilometer-resolution meteorological fields required over long forecast spans. Understanding the key mesoscale factors acting on the triggering, location, and intensity of the convective systems responsible for extreme accumulations is essential to gain insight into these episodes and contribute toward their accurate hydrometeorological forecasting. Mesoscale diagnosis suggests that local and distant orography, together with air–sea fluxes, were instrumental in developing convection and intensifying precipitation rate. Sensitivity experiments confirm the role of orography in organizing the cyclonic flow over the southeast part of the western Mediterranean, and also acting as a convection-triggering mechanism. Furthermore, results highlight the role of latent heat flux from the Mediterranean Sea in enhancing convective instability at lower levels and moistening the environment. These moist feeding flows substantially contribute to increasing precipitation rates. Such high sensitivity to environmental moisture distribution naturally propagates to the sea surface temperature, which, by means of sensible and latent heat flux exchanges, dominated the evolution of convective activity for the 12–13 September 2019 episode.

KEYWORDS: Mediterranean Sea; Convective storms/systems; Flood events; Numerical analysis/modeling

1. Introduction

Flash floods are among the most devastating natural hazards. They are responsible for high socioeconomic impacts, including human casualties and property loss and damage. The western Mediterranean littoral is characterized by the presence of steep small catchments that favor the development of flash floods. This, in combination with densely populated coastal areas, makes this region highly exposed. Indeed, estimated economic losses were EUR 34 billion between 1980 and 2015 (EU Floods Directive 2007/60/EC, https://www.eea.europa.eu/data-and-maps/data/european-past-floods). Coastal regions in northwestern Italy (e.g., Buzzi et al. 1998; Turato et al. 2004; Fiori et al. 2014), southeastern France (e.g., Sénési et al. 1996; Delrieu et al. 2005; Nuissier et al. 2008), and eastern Spain (e.g., Homar et al. 1999, 2002; García-Herrera et al. 2005) are flash flood–prone areas. The eastern coast of Spain is a remarkable example of a Mediterranean region persistently affected by heavy precipitation episodes (HPEs) resulting in flash flooding. Some historical examples are the episodes of 3 November 1987 in Gandia (València, eastern Spain) with 800 mm in 24 h (Llasat and Puigcerver 1994), 10 October 1994 with 400 mm in 24 h (Ramis et al. 1998), or 12 October 2007 with 400 mm in 24 h (Pastor et al. 2010).

In general terms, the most relevant mechanisms describing the genesis and evolution of deep moist convection in the region are well documented (e.g., Ramis et al. 1994; Doswell et al. 1998; Homar et al. 2002; Martín et al. 2007; Michaelides et al. 2018). The relatively warm Mediterranean Sea acts as a heat and moisture source during late summer and early autumn. Indeed, the maximum climatological frequency of flash flood producing HPEs occurs in autumn (e.g., Llasat et al. 2010). The combination of this factor with the presence of cold midlevel disturbances and maritime warm and moist air at low levels generates convective instability, identified by large convective available potential energy (CAPE). In addition, low-level jets over the sea and high moisture convergence are fundamental ingredients to develop deep convective activity. Indeed, moisture availability has proven crucial to produce convective unstable environments and sustain high precipitation rates (e.g., Pastor et al. 2015; Rainaud et al. 2017). This conceptual model was climatologically confirmed by Romero et al. (1999) and Martínez et al. (2008), who studied the synoptic patterns statistically associated with heavy precipitation in the Spanish Mediterranean region. These works link the presence of an upper-level trough over the western Mediterranean together with a northeasterly warm low-level flow to heavy accumulations in the mountainous regions of València, Murcia, and eastern Andalusia. Furthermore, the complex orography surrounding the western Mediterranean basin has a twofold effect: (i) acting as a

---

ⓞ Denotes content that is immediately available upon publication as open access.

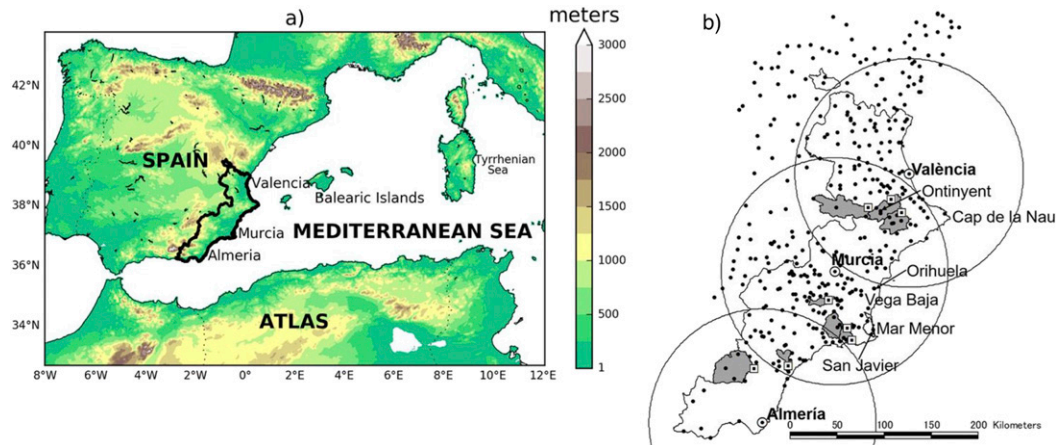*Corresponding author*: Alejandro Hermoso, alejandro.hermoso@uib.es

FIG. 1. (a) Computational domain used in the numerical simulation. The thick black line encloses the study area. (b) Location of the València, Murcia, and Almería radars (white dots) with respect to the selected catchments (light gray shaded areas). Circles of 120 km delineate the area covered by each radar. The 369 available automatic rain gauge stations are shown as black dots and automatic stream gauges are depicted as white squares. Geographical locations mentioned in the text are shown in both panels.

direct lifting mechanism (e.g., Buzzi et al. 1998; Ramis et al. 1998; Ducrocq et al. 2008; Bresson et al. 2012) and (ii) modifying the mesoscale flow (e.g., Homar et al. 1999). Orographic anchoring often produces quasi-stationary convective systems which may result in heavy precipitation persistence over individual basins. Indeed, these characteristics that contribute to sustaining large rainfall rates over long time spans make the Spanish Mediterranean a flash flood–prone region.

Identifying the key physical processes associated with the development, evolution, and intensity of convective systems is essential in order to produce more accurate quantitative precipitation forecasts (QPFs) and mitigate impacts from heavy precipitation and flash flooding in the Mediterranean basin. The investigation of individual case studies contributes to refine the conceptual model and account for smaller-scale processes that are expected to improve predictability and resilience against these devastating phenomena. Recent widespread availability of computational power enables the production of high-resolution simulations with a better representation of both topographic features and convective scale processes (Hohenegger and Schär 2007), and better complementing observation-based diagnostics. Nevertheless, the high nonlinearities involved in small-scale processes, such as convective flows and microphysical mechanisms, reduce the predictability horizon to a few hours (Zhang et al. 2015, 2016). Indeed, errors at convective-scale grow fast, eventually abating the diagnostic value of simulated fields at convective and subconvective scales. Coping with this fundamental limitation is key to advancing in the understanding of the physical processes and predictability of HPEs spanning several days.

The case under study took place on 11–14 September 2019, although the most intense precipitation occurred on 12–13 September. The 10-min precipitation accumulations exceeded 25 mm in several stations in Murcia (see Fig. 1 for the locations referred to in the text) during the first hours of 13 September (e.g., 32 mm in San Javier at 0400 UTC 13 September). Moreover, a maximum of 492 mm accumulated over 48 h was recorded in Orihuela. The subsequent widespread flash flooding across the València and Murcia regions produced devastating effects: seven casualties, the evacuation of hundreds of homes and estimated economic losses in excess of EUR 425 million (CCS 2019). The long period with deep convective activity combined with the wide extension of the affected area ($36\,700\,\text{km}^2$), which includes many small-to-medium catchments in the range between 100 and $1000\,\text{km}^2$, motivate an in-depth analysis of the physical mechanisms that determined the initiation, evolution, and intensification of the precipitation systems.

In this context, the Hydrological Cycle in the Mediterranean Experiment (HyMeX, https://www.hymex.org/) is an international program aimed, among other objectives, at improving the predictability of extreme weather events in the Mediterranean region (Drobinski et al. 2014). In particular, both parts of this study are framed within the "heavy rainfall, flash floods and floods" section of HyMeX, which addresses the following science questions: (i) What are the characteristics of extreme hydrometeorological events in the Mediterranean? (ii) How can heavy rainfall process knowledge and prediction be improved? (iii) How can flash flood hydrological prediction be improved? This part of the study tackles the first two questions. More specifically, the aim of this study is to improve the understanding of the relevant mesoscale and local-scale processes that act on the generation of persistent HPEs in the western Mediterranean. The case study selected exhibits singular aspects that provide a unique opportunity to better understand key processes acting across multiple spatial and temporal scales. During the long lifespan of this episode, multiple moisture sources may have concurred both to create convective instability in the lower troposphere and to feed the convective systems. The influence of the mesoscale and local-scale ingredients that contributed to the genesis and intensification of the convective systems is analyzed in detail by means of observational diagnostic and numerical sensitivity experiments.

The identification of crucial mechanisms acting on the development and evolution of these systems is essential to increase the ability of hydrometeorological chains to generate valuable high-resolution and accurate flood forecasts for civil protection agents. The study of hydrometeorological predictability by means of advanced ensemble generation strategies is discussed in Amengual et al. (2020, manuscript submitted to *J. Hydrometeor.*, hereafter Part II).

The rest of the paper is structured as follows: section 2 describes the episode using all available observations, including synoptic analysis, satellite and radar polar volumes, and rain gauge recordings. Numerical experiments are described in section 3, and results are discussed in section 4. The main conclusions and further remarks are presented in section 5.

2. Diagnostic of the episode

Since the episode affected coastal areas, the number of relevant available in situ observations is very scarce. Operational analyses from the European Centre for Medium-Range Weather Forecasts (ECMWF) represent the synoptic pattern, whereas satellite and radar information reveal characteristics of the mesoscales and convective scales that help link the intense accumulated precipitations with convective activity.

a. Synoptic situation

On 9 September, the synoptic situation featured a prototypical setting with a prominent trough at mid- and upper levels. The subsequent formation and southward progression of a deep trough with a closed cutoff affected the Iberian Peninsula from 10 September. Later on, an intense PV streamer with values exceeding 6 PVU (1 PVU = 10^{-6} K m^2 s^{-1} kg^{-1}) is identified until 1200 UTC 11 September. At this time, the trough was already cut off from the main synoptic wave and continued advancing southward over Algeria, where it remained nearly stationary on 12 and 13 September (Fig. 2a).

At low levels, the situation on 10 September was characterized by a high pressure system over the North Atlantic and the formation of a depression over the western Mediterranean. This cyclone intensified the northeastern flow toward the Spanish Mediterranean coastlands during the first hours of 11 September. The following days, the depression shifted south steered by the upper-level cutoff and merged within a larger North African low pressure region. This low—in combination with the North Atlantic high that had extended toward the north of Europe—produced an easterly flow over the western Mediterranean (Fig. 2b). Undulations in the sea level pressure field north of the Atlas mountain range suggest an orographic lee cyclogenesis effect that modulated the general easterly flows as they impinged on the Spanish Mediterranean area (not shown).

b. Mesoscale and local-scale settings

Three distinct phases of the episode naturally arise from the analysis of the mesoscale and local-scale processes:

- Phase 1 (0000–0600 UTC 12 September): Cyclonic easterly flow and an associated warm front dominated the mesoscale environment over the southwestern sector of the western Mediterranean basin during the first hours of 12 September.
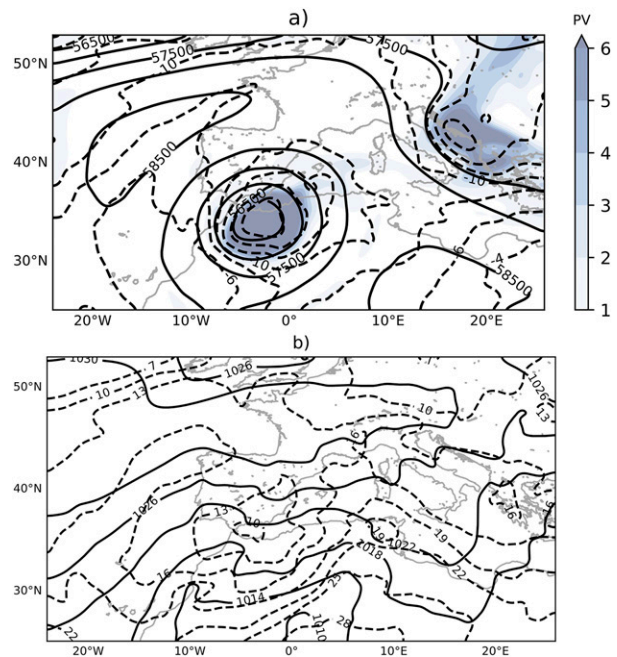

FIG. 2. ECMWF analyses valid at 1200 UTC 12 Sep 2019 of (a) geopotential (m^2 s^{-2}; solid line), temperature (°C; dashed line) at 500 hPa, and 250-hPa potential vorticity (PVU; shaded) and (b) sea level pressure (hPa; solid line) and temperature (°C; dashed line) at 850 hPa.

Dense cloud cover is identified along the strongest warm advection areas off the Algerian coast and along the southeast coast of Spain. The thermodynamic environment at low levels was characterized by a warm front over Algeria moving westward, and an elongated area of high equivalent potential temperature θ_e, which extended from Sardinia to the Iberian Peninsula (Fig. 3a). This warm and moist air was advected westward, curling around the cyclonic flow during the subsequent hours. This flow combined with the influence of the cold upper-level cutoff brought moisture toward the València region and produced convective instability, with CAPE values around 500 J kg^{-1} (Fig. 4a). A persistent and elongated area of anchored convection originated over an area of significant elevations in the Cap de la Nau (e.g., Serra del Penyal with peaks exceeding 840 m at distances of 10–15 km from the coastline, Fig. 5a). This type of persistent convective activity is frequent over mountainous ranges in the Mediterranean region as well as in other regions worldwide, giving rise to quasi-stationary precipitation over particular locations (e.g., Cosma et al. 2002; Kirshbaum et al. 2007).

- Phase 2 (0600–1800 UTC 12 September): The abovementioned elongated area of instability over the sea moved southward, while the warm front advanced westward (Fig. 3b). Consequently, an area of high convective instability with CAPE exceeding 1000 J kg^{-1} over Vega Baja and the nearby maritime strip was produced (Fig. 4b). Convergence of the low-level easterly flow with outflows from previous convective activity supported the triggering of individual cells over the sea (Fig. 5b). During the afternoon of 12 September,
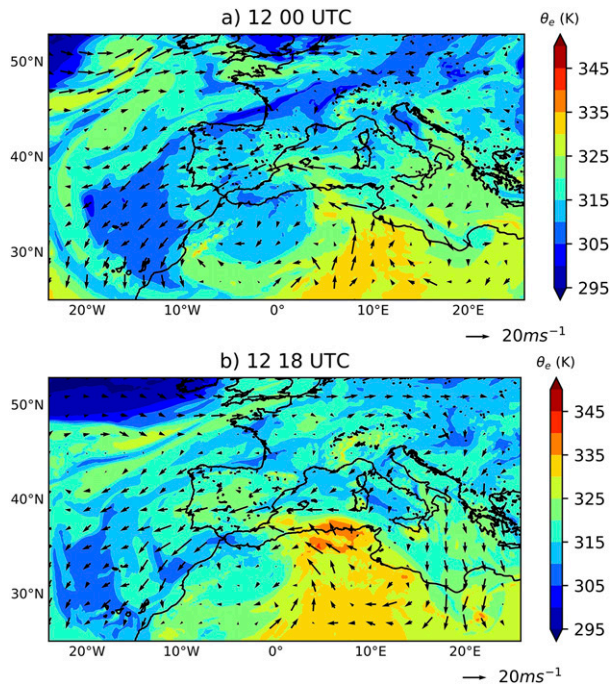
FIG. 3. Equivalent potential temperature θ_e (contoured colors; K) and wind speed (arrows) at 850 hPa from the ECMWF analyses valid at (a) 0000 and (b) 1800 UTC 12 Sep 2019.

high convective instability over the Mediterranean Sea, south of the Balearic Islands (Fig. 4c), favored convection development in North Africa and over the sea. As a result, a prominent convective system formed in front of the southern coast of València.
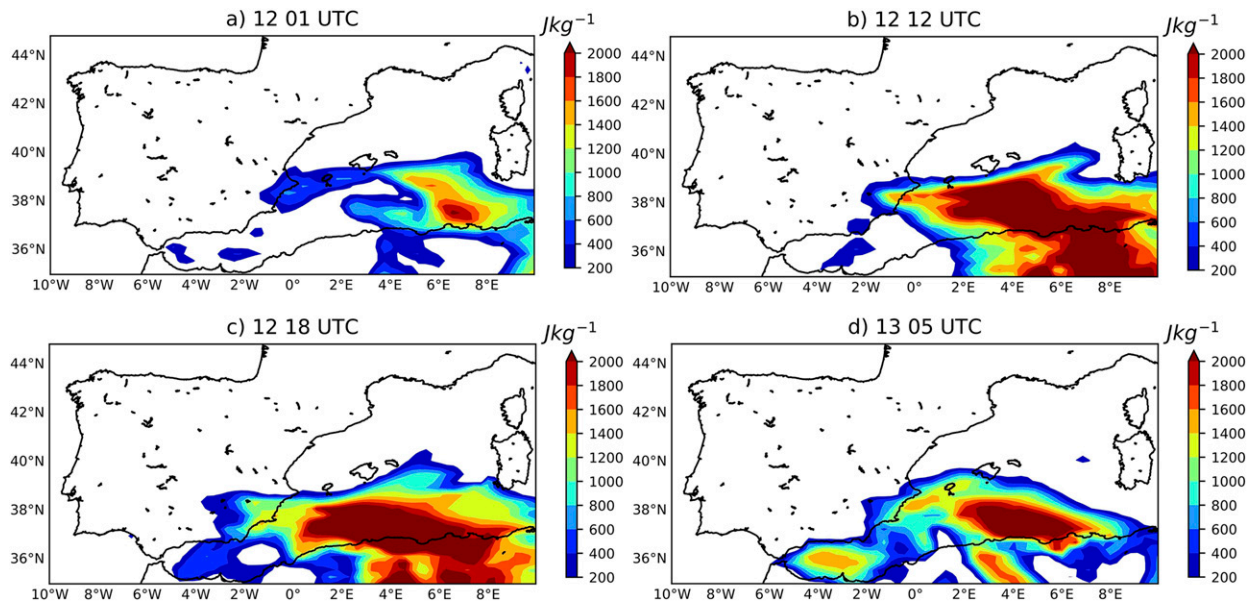
- Phase 3 (1800 UTC 12 September–1200 UTC 13 September): During the last hours of 12 September, scattered cells were triggered near the Murcia coastline and merged with the aforementioned organized system. Continuous θ_e advection promoted the generation of new convective cells, forming a mesoscale convective system (MCS; Fig. 5c), with a characteristic "V" shape on infrared satellite images (not shown). Orographic anchoring produced by the significant elevations surrounding Mar Menor, with heights over 600 m, may have contributed to the stationarity of the MCS formed in the area. Afterward, the northeasterly flow toward Murcia veered northward, in phase with the progression of the cutoff low. The area of convective instability extended into Cap de la Nau (Fig. 4d), producing convective activity from 0500 UTC 13 September (Fig. 5d).

c. Radar quantitative precipitation estimates and analysis

The automatic rain gauge database considered consists of 369 stations, with a density of nearly 1 station per 100 km^2 in the area of interest (Fig. 1b). These observations enable monitoring of pluviometric evolution and calibration of radar precipitation estimates. Furthermore, 227 additional rain gauges with daily recordings are also available (Fig. 6b).

Precipitation estimates are derived from the reflectivity volume scanning of the Almería, Murcia, and València Doppler C-band radars at 0000 UTC 12–14 September. Each individual weather radar completes a volume-scanning at 1-km spatial resolution every 10 min with a maximum radar range of 240 km. Partial beam occlusion is corrected by carrying out numerical simulations of the percentage of beam power intercepted by the orography (Pellarin et al. 2002), while signal attenuation by heavy rain is amended by applying the Mountain Reference Technique (Bouilloud et al. 2009). The standard WSR-88D

FIG. 4. Convective available potential energy (CAPE; contoured colors; J kg^{-1}) from ERA5 reanalyses valid at (a) 0100, (b) 1200, (c) and 1800 UTC 12 Sep 2019, and (d) 0500 UTC 13 Sep 2019.
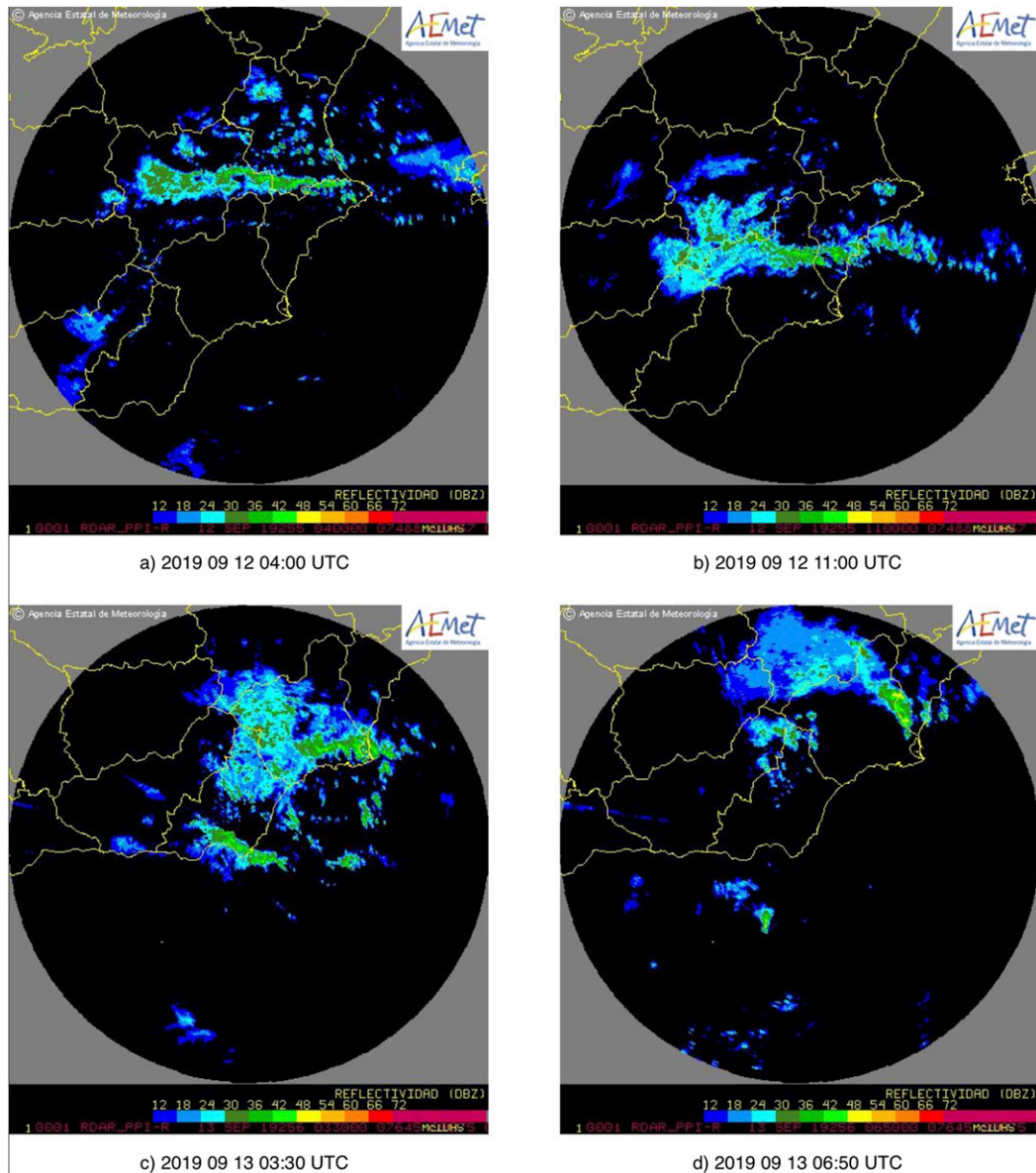
FIG. 5. Reflectivity images from the Spanish Meteorological agency radars. Images of Murcia radar valid at (a) 0400 and (b) 1100 UTC 12 Sep 2019, and from Almería radar at (c) 0330 and (d) 0650 UTC 13 Sep 2019.

convective rainfall rate–reflectivity relationship (i.e., $Z = 300R^{1/4}$; Hunter 1996; Fulton et al. 1998) is applied to derive quantitative rainfall estimates. Considering the large uncertainties associated with radar quantitative precipitation estimation (e.g., Gochis et al. 2015), additional biases in the precise hourly rainfall amounts and spatial distributions are corrected by using a dynamical adjustment based on automatic rain gauge data (Cole and Moore 2008). An independent verification test is carried out over the region of interest after the correction of errors in the hourly radar-derived rain. This quality check is performed by comparing the 48-h accumulated radar precipitation estimates against cumulative values recorded at the 227 independent daily rain gauges (Fig. 6). Statistical comparison between both

databases shows a strong positive correlation, with a squared correlation coefficient of 0.88. Radar estimates are slightly negatively biased, with a mean underestimation of 11.1%.

According to the radar estimates, 48-h rainfall accumulations were above 500 mm in some areas (Fig. 6b). The impacts of the convective systems are well captured for the three phases of the episode.

• Phase 1: Torrential precipitation was mainly recorded in the southern Valencian region, with a 6-h accumulation of 210 mm and a maximum 10-min intensity of 16 mm in the Ontinyent rain gauge (Fig. 1b). The signature of the thin convective band is clearly visible in radar rainfall estimates (Fig. 7a). This structure persisted for approximately 6 h.
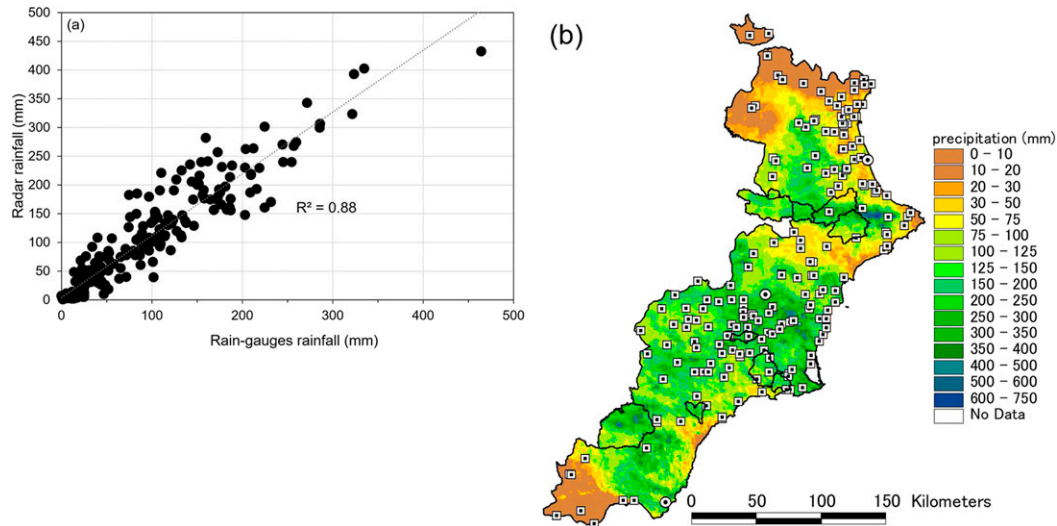
FIG. 6. (a) Scatterplot of the 48-h radar estimates against accumulations by the daily rain gauge network and (b) spatial distribution of the 48-h accumulated radar-estimated precipitation from 0000 UTC 12 Sep to 0000 UTC 14 Sep 2019 over the study region. Thick black lines denote hydrographic basins. White squares stand for daily rain gauges. White dots show the position of weather radars.

• Phase 2: Intense precipitation took place over Vega Baja, with a record of 180 mm in 2 h, between 0900 and 1100 UTC. Peak 10-min intensity was above 20 mm in Orihuela, corresponding to a linear structure (Fig. 7b). In the afternoon, moderate precipitation intensities affected mainly southern València and western Murcia (Fig. 7c).

• Phase 3: The most intense systems formed during this phase, affecting southeast Murcia and Vega Baja with hourly intensities of 146 mm over San Javier. Furthermore, 10-min recordings over southeast Murcia exceeded 30 mm between 0330 and 0430 UTC, the period of most intense convective activity, corresponding to the mature stage of the quasi-stationary MCS identified. In addition, intense convective band activity affected western Almería with maximum 6-h accumulations above 200 mm (Figs. 7d,e). From 0500 UTC 13 September, the precipitating system moved northward, again affecting Vega Baja with similar intensities to phase 2. Cap de la Nau was also impacted, with lower rainfall amounts than phase 1 (Fig. 7f).

The torrential features of this HPE are examined by means of the relationship between maximum 30-min rainfall intensities and total rainfall amounts, and the fraction of total precipitation with 30-min intensities > 20 mm h^{-1}. Both metrics are commonly used to regionally characterize rainfall conducive to flash flooding, highlighting intense precipitation rates and stationarity (Borga et al. 2007). Stations located inside the catchments (Fig. 1b) are selected and arranged in three groups: northern, central, and southern basins, comprising 39, 60, and 22 rain gauges, respectively.

Northern and central basins were affected by the most intense and largest convective precipitations during phases 1 and 3 (Fig. 8). The high values of the total precipitation fraction with strong intensities reveal the quasi-stationary character of

the rainfall. A striking characteristic of this HPE is that some automatic stations were under major convective rainfall for most of its entire duration. Sixty percent of cumulative precipitation exceeding 300 mm at eight rain gauges in the northern and central basins was under heavy rainfall rates. Precipitation affecting the southern watersheds was of the same extreme nature, but shorter. These metrics clearly indicate the potential for flash flooding.

Accurately predicting the flash floods associated to these HPEs is highly dependent upon a precise spatial and temporal distribution of quantitative precipitation forecasts. A comprehensive description of distinct ensemble prediction strategies coping with the different sources of uncertainty that usually restrict precise flash flood forecasting is presented in Part II. The most interesting particularities of this case study are related to the local scale. The complex orography of the region is responsible for the anchoring and organization of the highly efficient convective cells. Furthermore, this episode had a long duration when compared to the usual time span of HPEs in the Mediterranean region and other areas (1 day or less; Marchi et al. 2010; Amponsah et al. 2018; Dougherty and Rasmussen 2019).

When comparing the 12–13 September 2019 HPE with other similar cases over the study region, the large-scale environment was comparable to the 21–24 October 2000 episode (Homar et al. 2002), but with different sub-synoptic-scale mechanisms, which yielded a different precipitation distribution. The first phase was similar to the 12 October 2007 case (Pastor et al. 2010), with a northeasterly flow over Cap de la Nau. However, in the September 2019 case, the area affected by intense precipitation was larger due to the change of the easterly flow to southeasterly, conveying unstable air to the Murcia region at a later stage. Furthermore, this case study presents different convection triggering mechanisms: orographic outset (e.g.,
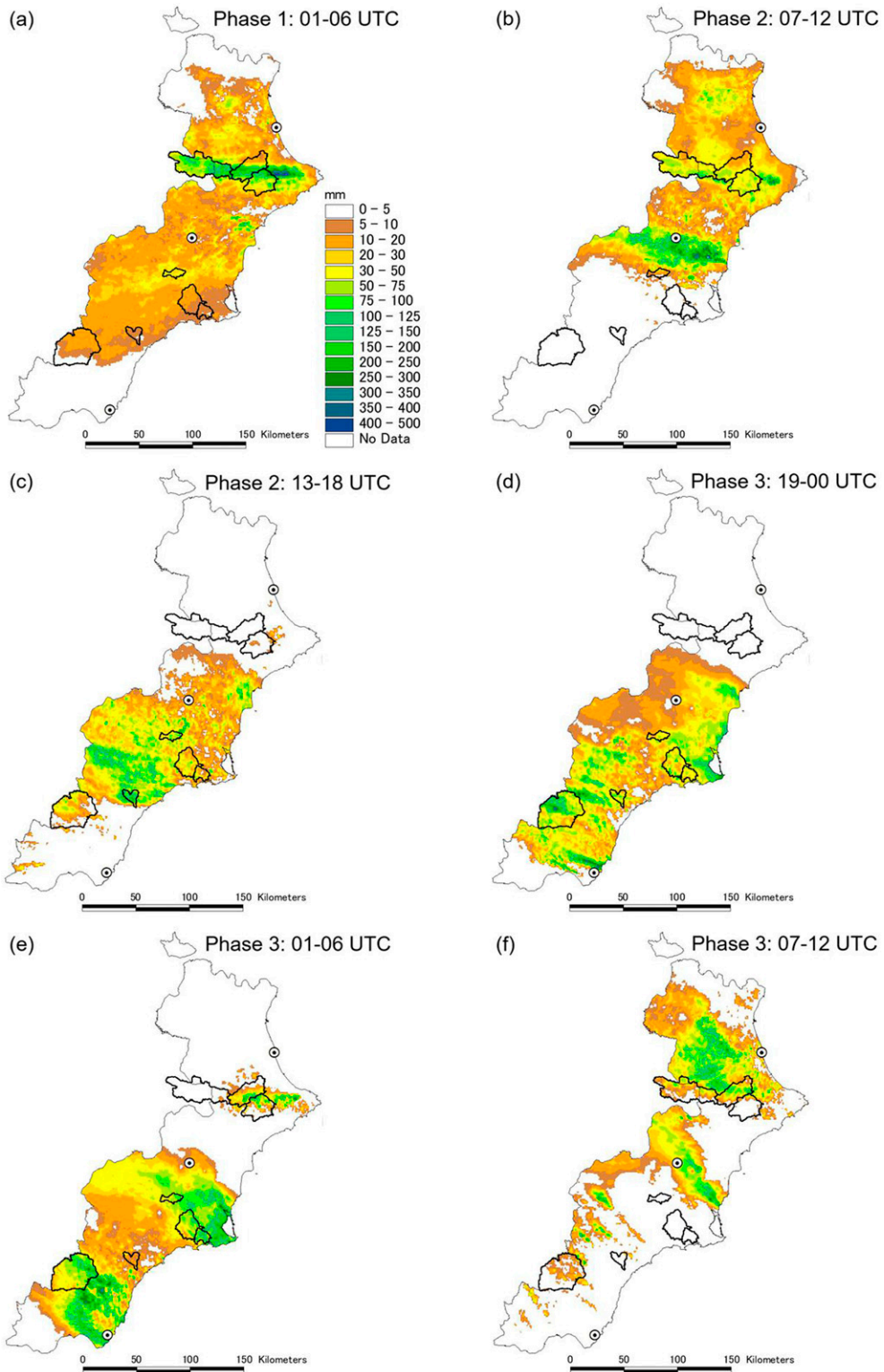
FIG. 7. Spatial distribution of 6-h accumulated radar-estimated precipitation corresponding to (a) 0100–0600, (b) 0700–1200, and (c) 1300–1800 UTC 12 Sep 2019; (d) from 1900 UTC 12 Sep 2019 to 0000 UTC 13 Sep 2019; and (e) 0100–0600 and (f) 0700–1200 UTC 13 Sep 2019. Thick black lines denote hydrographic basins. White dots are the positions of weather radars.
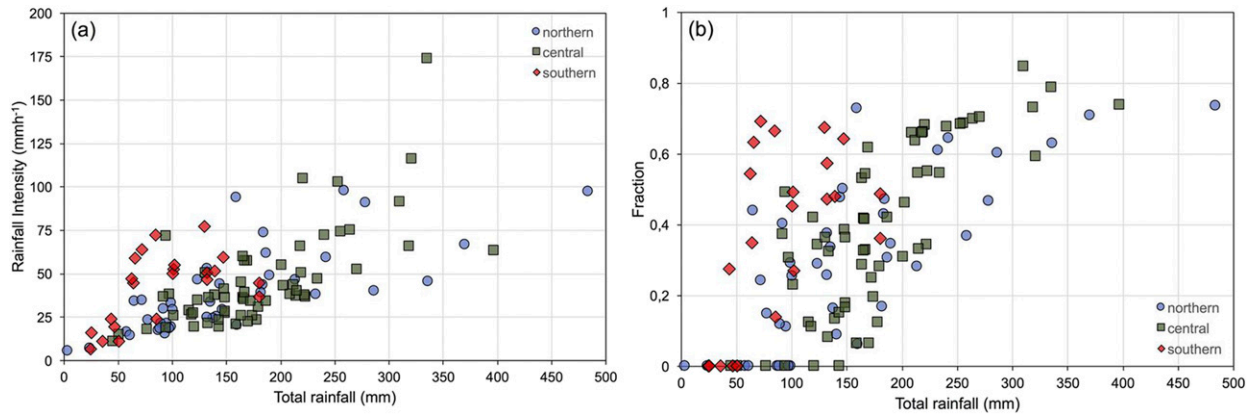
FIG. 8. Scatterplots of (a) total rainfall amounts vs maximum 30-min rainfall rates and (b) total rainfall amounts vs fractions of the total amounts produced by heavy precipitation rates (i.e., 30-min rainfall rates exceeding 20 mm h^{-1}) from 0000 UTC 12 Sep to 0000 UTC 14 Sep 2019 for automatic rain gauges located inside northern (blue circles), central (green squares), and southern (red diamonds) catchments.

Ramis et al. 1998) in phase 1, with initiation over the sea (e.g., Homar et al. 1999) in phases 2 and 3. This diversity in triggering mechanisms and local-scale phenomena encourages a further exploration by means of numerical simulations in order to improve some aspects of the conceptual model of HPEs in the western Mediterranean, especially with regard to features related to small-scale processes.

3. Numerical experiments

Numerical experiments in this study are designed to generate a high-resolution description of the conditions that favored and sustained the HPE. After a qualitative assessment of the control run, the effect of the most important factors detected in the observational analysis is quantified by means of sensitivity experiments.

a. Control run

The relevance of the findings obtained from sensitivity experiments is conditioned by the availability of an accurate control simulation. In this sense, the control simulation must reproduce, to a large extent, the most relevant features identified in the observational diagnostic. Numerical experiments are performed with the Advanced Research core of the Weather Research and Forecasting (WRF-ARW) Model version 3.9.1.1 (Skamarock et al. 2008). A single computational domain covering the entire western Mediterranean basin is defined (Fig. 1a). This domain has 2.5 km horizontal resolution (750 × 500 grid points) and 50 vertical terrain-following η levels up to 50 hPa. The evaluation period covers 48 h from 0000 UTC 12 September to 0000 UTC 14 September. However, simulations start at 1800 UTC 11 September to allow for a spinup period after a cold start, which is especially critical for precipitation processes (e.g., Sun et al. 2012). This forecast period comprises the entire duration of the episode and is adequate to analyze the impact of the different physical mechanisms assumed to be relevant after the observational diagnostic, such as the role of local and distant orography or sources of moisture. Physical parameterizations

of the simulation include: the NSSL 2-moment microphysics (Mansell et al. 2010), RRTMG radiation scheme (Iacono et al. 2008), Mellor–Yamada and Nakanishi–Niino level 2.5 PBL (Nakanishi and Niino 2006), and RUC land surface model (Smirnova et al. 2016), while convection is not parameterized. The 2.5-km horizontal resolution explicitly represents a major part of convective activity, although it is still in the so-called gray zone, as some important processes for the simulation of convection, such as in-cloud turbulence are not fully resolved. However, convection parameterization at this resolution has been shown to perform poorly, especially for heavy precipitation (e.g., Han and Hong 2018), while a successful representation of deep moist convection without the use of convective parameterizations has been obtained for resolutions higher than 4 km (e.g., Kain et al. 2008; Weisman et al. 2008). This model configuration, as well as the initial and lateral boundary conditions (IC/LBCs) are taken from one ensemble member out of all the ensemble strategies investigated in Part II. In particular, the boundary conditions are extracted from the global ECMWF ensemble prediction system and soil parameters are downscaled from the control member of the ECMWF ensemble. ICs are obtained by applying the tailored bred technique (Hermoso et al. 2020; BV in Part II) to perturb the control member of the ECMWF ensemble. This member was chosen after a qualitative comparison of the simulated convective activity against radar reflectivities over the entire HPE. The selected member captures the observed evolution adequately enough to serve as a basis for a physical study of the episode.

The control run reproduces the synoptic evolution accurately, positioning the cold cutoff low over North Africa during 12 September. The easterly flow advecting warm and moist air into the València and Murcia regions during 12 September is also identified throughout the simulation (Fig. 9). High θ_e values at low levels are found in the western Mediterranean, together with the warm front moving westward and reaching the Iberian Peninsula. Intense convective instability dominates the western Mediterranean on 12 and 13 September, with maximum CAPE values above 2000 J kg^{-1}. The main features
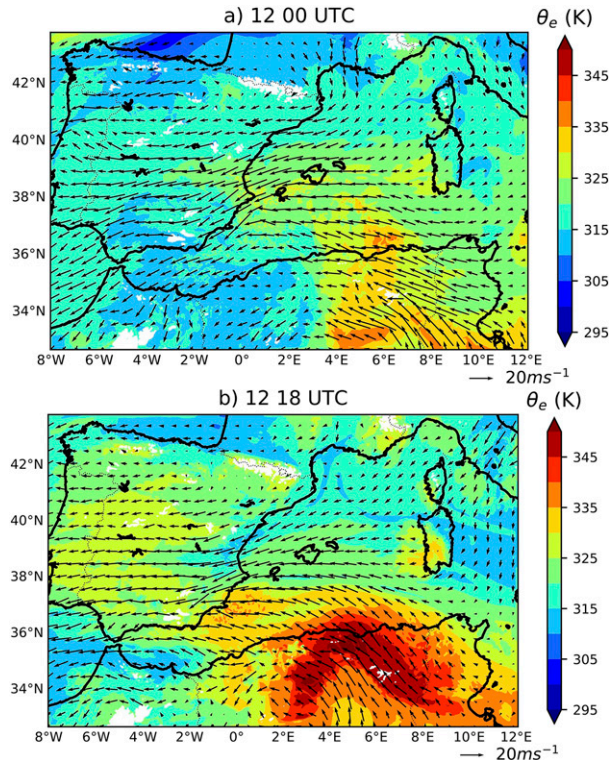
FIG. 9. Equivalent potential temperature (contoured colors; K) and wind (arrows) at 850 hPa for the control simulation at (a) 0000 and (b) 1800 UTC 12 Sep 2019.

of CAPE are consistent with ERA 5 (Fig. 4), but with higher simulated values exceeding 1000 J kg^{-1} during the first hours of 12 September. An area of strong instability extending from the south of Sardinia up to Cap de la Nau is found (Fig. 10a), in agreement with ERA5. This unstable air mass progresses southward affecting southern València and Murcia regions (Fig. 10b), slightly further south than ERA 5. This minor southward shift continues during the afternoon of 12 September, rendering more stable air over land (Fig. 10c). On 13 September, the simulated CAPE evolution is coherent with ERA 5, with more unstable air over the sea during the first hours (Fig. 10d).

Regarding precipitation, the 48-h simulated accumulation reproduces the most relevant features of the observed rainfall distribution. Intense precipitation is found in the València region, near Cap de la Nau, although it is weaker than radar-derived cumulative rainfall. The control run also renders accumulations above 500 mm, although slightly displaced to the south with respect to the radar-derived cumulative rainfall (Fig. 11). Phase 1 is fairly well captured by the control run, although the thin linear precipitation structure is not accurately simulated. Thus, simulated rainfall amounts are lower than observed: 6-h maximum accumulations around 100 mm and above 200 mm, respectively (Fig. 12a). Even though a linear structure similar to the one observed is simulated by the control run over Vega Baja in phase 2, accumulations are underestimated, with rainfall values below 100 mm, while recorded quantities reached 200 mm at some locations. During

phase 3, rainfall exceeds 250 mm near Mar Menor during the first hours of 13 September. However, heavy precipitation in southeast Murcia begins slightly earlier than observed, during the last hours of 12 September, and precipitation produced in southern València during the afternoon of 12 September is displaced to the south in the control experiment (Fig. 12c). Convective activity persists and, similarly to observations, a MCS organizes affecting Murcia, with notable intensities over the Mar Menor area (Figs. 12d,e). Convective bands over western Almería are northwardly shifted and are less intense and shorter than observed. The subsequent northward evolution of the MCS enters the València region in the final stage (Fig. 12f), with 6-h accumulations over the sea above 100 mm. The intense CAPE found over marine areas in the simulation (Fig. 10d) favors convective activity and extreme rainfall.

In brief, the control run reproduces with reasonable accuracy the main synoptic and mesoscale processes acting over the entire HPE. As a consequence, this simulation qualifies as a reference to both conduct a high-resolution diagnostic and sensitivity experiments so as to distill additional quantitative information regarding the effects of the specific physical factors acting in this singular case.

b. Sensitivity experiments

Although the basic mechanisms acting on HPEs over the western Mediterranean are generally well established, diagnosis of both the available observations and simulated fields for this episode elicits questions concerning the specific role of each physical factor in the timing, location, and intensity of the extreme precipitation fields. Two important factors detected are (i) orography, especially at the local scale, which was important in triggering and anchoring convection throughout the episode, and (ii) the high moisture content at low levels. The latter requires a distinction between moisture supplied by evaporation from the sea with respect to the water vapor already present at low levels at the beginning of the episode.

1) OROGRAPHIC FACTORS

The prominent complex topography surrounding the western Mediterranean Sea is decisive in organizing mesoscale flows in severe weather events (e.g., Homar et al. 1999; Davolio et al. 2009; Buzzi et al. 2014; Demirtaş 2016). The role of remote orography (i.e., mountain ranges distant from the study area) in this episode is investigated with the NOATLAS experiment, in which the Atlas range is flattened in the numerical simulation (Table 1 for a list of experiments run in this study).

Furthermore, uplifts or convergent areas generated by local orography are frequent triggering and/or anchoring mechanisms for convective precipitation systems during torrential episodes in the region (e.g., Homar et al. 2003). The NOLORO experiment quantifies the influence of these local small-scale mechanisms on the generation and evolution of convective activity. To this end, the orography is modified as follows:

$$\text{ORO*} = \text{ORO}[1 - G(\mathbf{x}_{\text{max}}, \sigma)], \qquad (1)$$

where ORO* is the modified orography, ORO is the original model orography, and $G(\mathbf{x}_{\text{max}}, \sigma = 225\,\text{km})$ is a two-dimensional
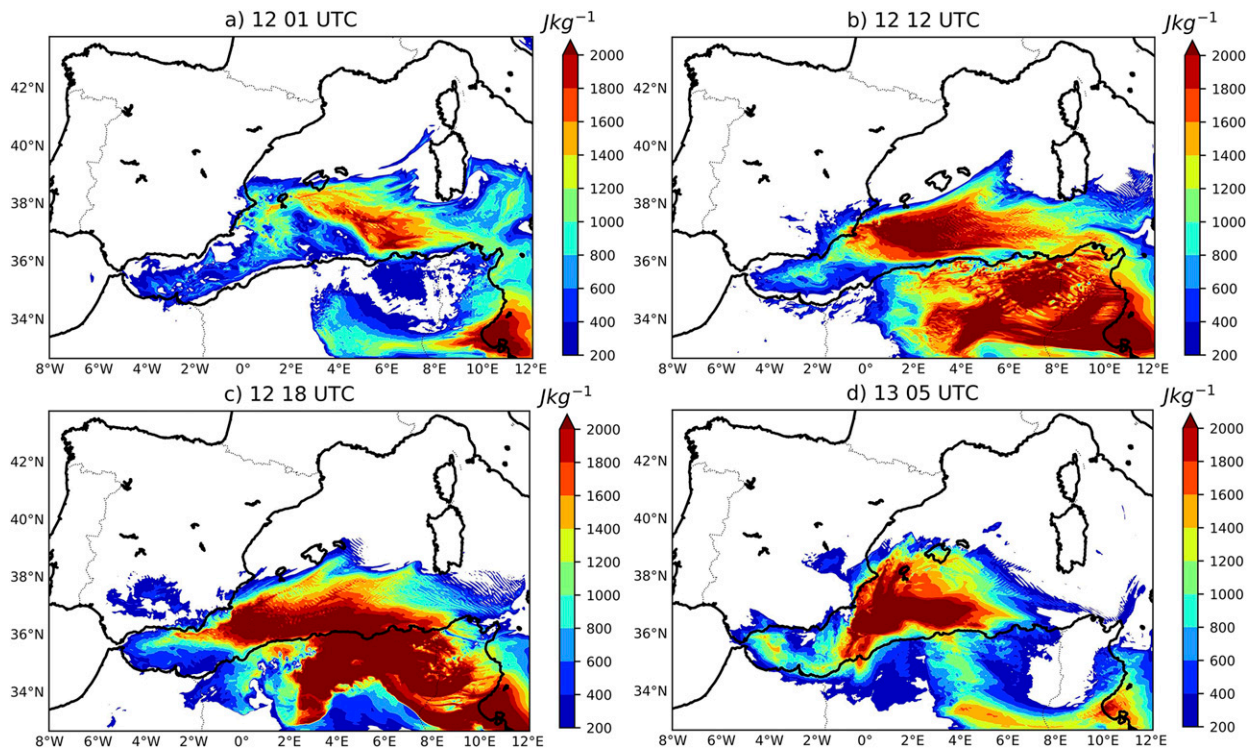
FIG. 10. Convective available potential energy for the control simulation at (a) 0100, (b) 1200, and (c) 1800 UTC 12 Sep and (d) at 0500 UTC 13 Sep.

Gaussian centered at $\mathbf{x}_{max}$ = 37.7°N, 0.74°W. This point is located over southeast Murcia, where persistent precipitation enhanced by orographic anchoring was observed. This definition enables prominent mountain ranges to be partially smooth out, without abrupt discontinuities in height as the orographic modification tends to zero for distant points. This value of σ generates a perturbation covering the study area, with higher relative modifications near the area where the quasi-stationary MCS produced intense precipitation.

Admittedly, these experiments still contain marginal information of the orographic features removed through the IC/LBCs. However, their effect is assumed to be residual after the 6-h spinup time.

2) WATER VAPOR SOURCES

The moisture content required to develop and sustain deep moist convection can originate from multiple sources. Duffourg and Ducrocq (2011) showed that the humidity contributing to HPEs in the western Mediterranean is confined in the lowest 1000 m and mainly originates from evaporation from the Mediterranean Sea, although large amounts of humidity can come from additional remote sources.

Evaporation is an ever-present candidate factor when investigating HPEs in the Mediterranean region (e.g., Lebeaupin et al. 2006; Pastor et al. 2015; Ivatek-Šahdan et al. 2018). The high values of latent heat flux identified in the control simulation over the western Mediterranean throughout the episode underline its importance. The impact of evaporation from the sea is assessed by switching off this process in the NOLHF

experiment. Similar to the orographic factor, IC/LBCs are also influenced by surface evaporation. Indeed, in a strict sense, this experiment only investigates the effect of maritime surface latent heat flux over the domain and during the simulation time span.

On the other hand, the easterly and northeasterly low-level flow over the western Mediterranean may have been an efficient conveyor belt of moisture already present in the lower troposphere toward the eastern Spanish coasts at the unfolding of the episode. To better disentangle the origin of moisture,
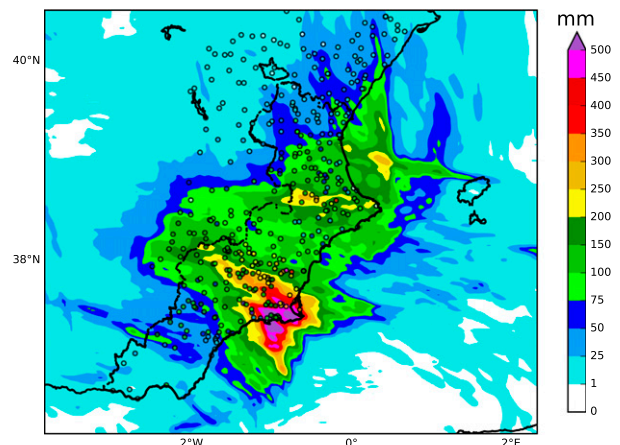

FIG. 11. 48-h accumulated precipitation for the control simulation and rain gauge stations from 0000 UTC 12 Sep to 0000 UTC 14 Sep.
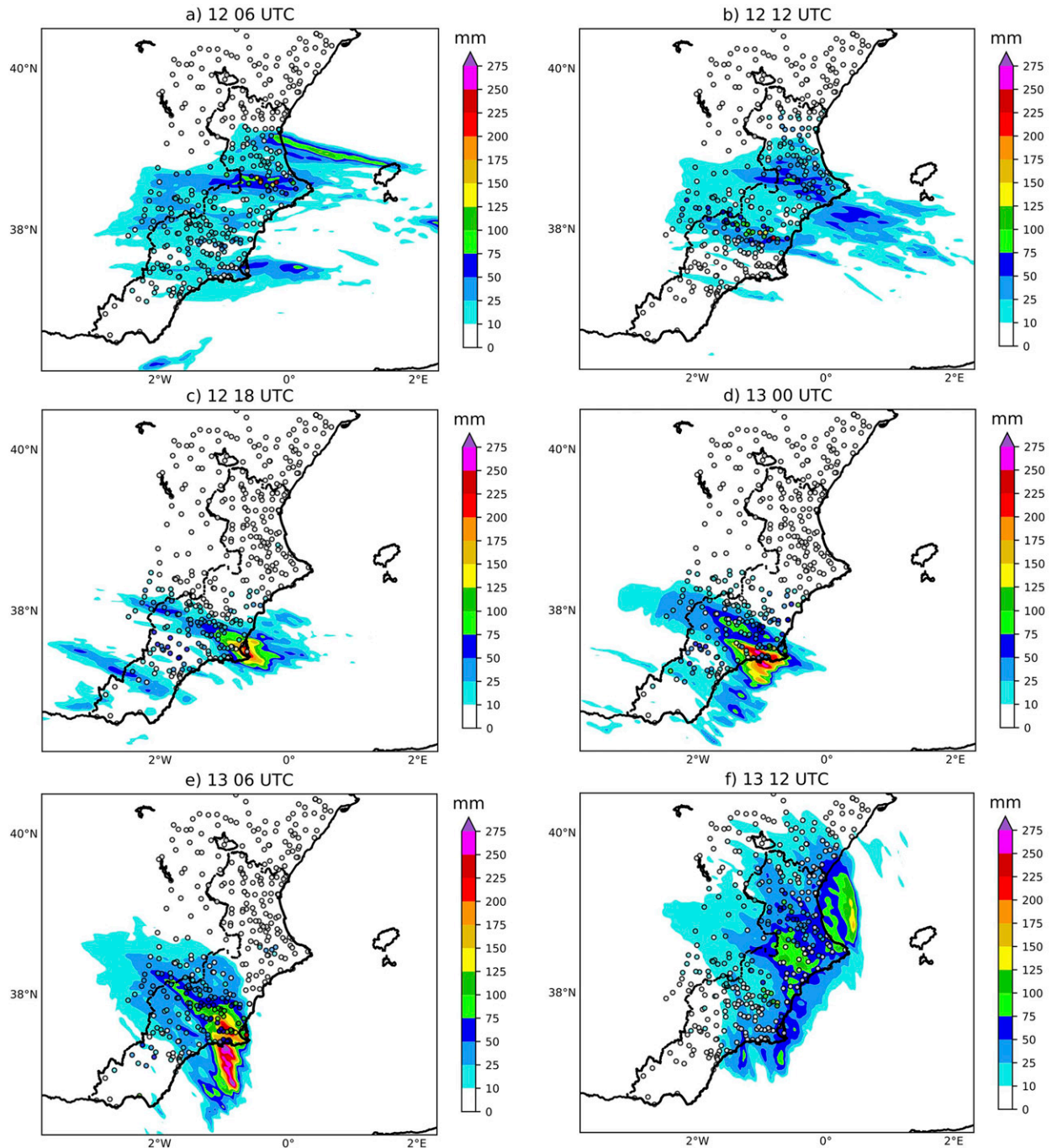
FIG. 12. 6-h accumulated precipitation for the control simulation (shaded) and rain gauge stations (dots) at (a) 0600, (b) 1200, and (c) 1800 UTC 12 Sep, and at (d) 0000, (e) 0600, and (f) 1200 UTC 13 Sep.

a sensitivity experiment keeping the original surface exchange fluxes, but with drier ICs than CNTL over the Tyrrhenian Sea (labeled QMOD) is also designed. The modification is applied to all model levels by using a similar perturbation procedure to NOLORO:

$$Q^* = Q[1 - 0.5G(x_c, y_c, \sigma_x, \sigma_y)], \qquad (2)$$

where Q is the original specific humidity in the ICs, and G is a Gaussian centered in (x_c, y_c). The central point is 38.89°N, 7.61°E (maritime point, southwest of Sardinia), and the standard deviations are approximately 170 and 115 km in the west–east and south–north directions, respectively. This perturbation encompasses an area of high specific humidity at 1800 UTC 11 September over the Tyrrhenian Sea and

TABLE 1. Summary of the different sensitivity tests: 1 indicates that the factor is switched on and 0 otherwise. For SST experiments, modification in the SST field (°C) is specified.

Experiment name	Atlas	Local orography	Latent heat flux	SST	Specific humidity Tyrrhenian Sea
CNTL	1	1	1	0	1
NOATLAS	0	1	1	0	1
NOLORO	1	0	1	0	1
NOLHF	1	1	0	0	1
QMOD	1	1	1	0	0
SST − 1	1	1	1	−1	1
SST + 1	1	1	1	+1	1

extends over the western Mediterranean, where a high θ_e area is identified.

3) SEA SURFACE TEMPERATURE

Sensible heating can also contribute to convectively destabilize the lower troposphere. In addition, air–sea fluxes can modify the interaction between low-level flow and topography, or even promote maritime convective triggering (Stocchi and Davolio 2017). Sea surface temperature (SST) is a critical field for air–sea exchange processes. To specifically investigate the influence of SST on the thermodynamic environment and moisture availability, a set of experiments with a uniform change in SST is designed. Experiment labeled as SST − 1 features a sea surface temperature 1°C lower than the analysis used in CNTL from ECMWF. This SST analysis field is taken from the global, high-resolution, operational sea surface temperature and sea ice analysis system (OSTIA; Stark et al. 2007; Mogensen et al. 2012). Analogously, a positive perturbation is introduced in the SST + 1 experiment.

4. Results

a. High-resolution diagnostic

1) PHASES 1 AND 2: CONVECTION-CONTRIBUTING MECHANISMS

The reliable control simulation complements the observational diagnostic with higher resolution numerical information. A high moisture convergence area at low levels was present near Cap de la Nau during the first hours of 12 September (Fig. 13a). The confluence of a northeasterly and an easterly low-level jets advected high θ_e air over this area, feeding the thin convective band which developed over Cap de la Nau as well as the subsequent linear structure developed during phase 2. Indeed, a positive anomaly of θ_e was found over the sea generating convective instability at the beginning of phase 1 (Fig. 13a). Furthermore, the low-level convergence supported upward motion and the triggering of new convective cells that boosted the maintenance of the thin convective band. In addition, this region is favorable to orographic uplift, suggesting the important role of local topography in the development of precipitation.

During phase 2, the southward evolution of the warm and moist air mass favored the convective development that led to
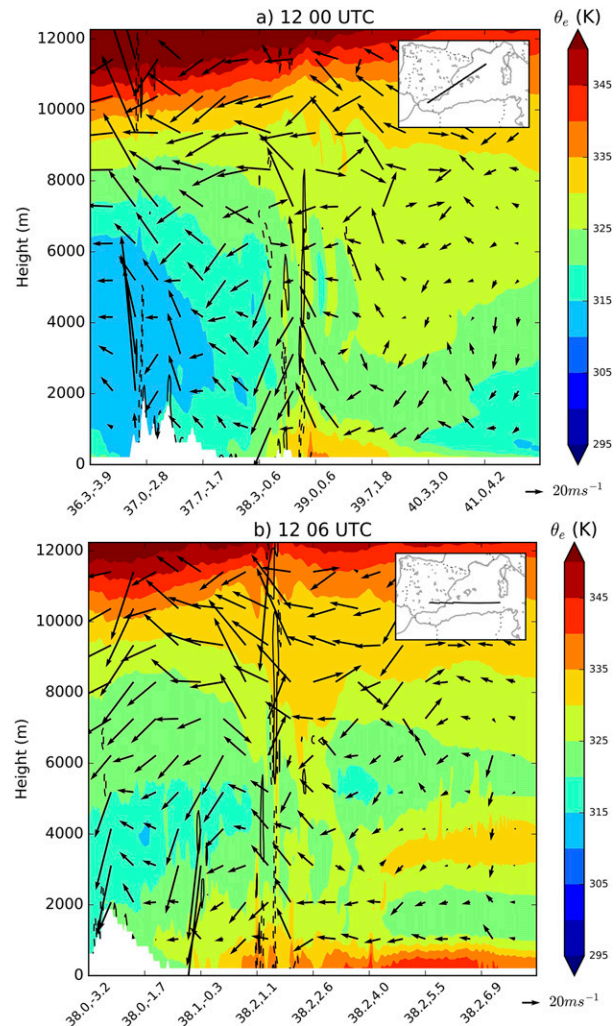

FIG. 13. Vertical cross sections of equivalent potential temperature (contoured colors), wind speed (arrows), and divergence (convergence) greater than 0.001 s^{-1} represented by solid (dashed) black lines for the control simulation at (a) 0000 and (b) 0600 UTC 12 Sep 2019. The scale for vertical wind is 100 times larger than the horizontal scale. Top-right inset maps depict the position of the cross section, chosen to be approximately parallel to the 850-hPa wind in the region of interest.

the unfolding of the linear structure. Convergence over the sea (Fig. 13b) promoted upward motion and the development of convective cells that eventually organized over land forming the structure identified in the observational diagnostic.

2) PHASE 3: MCS FORMATION AND MAINTENANCE

During the last hours of 12 September, the flow veered to southeast, bringing warm and moist air into Murcia. CAPE values were well above 1000 J kg^{-1}, supporting an environment for convective initiation. Convergence over the sea contributed to upward forcing and subsequent triggering of convective cells that ultimately caused the intense precipitation observed during phase 3. The vertical profile of θ_e clearly signals the presence of this convective activity over the sea. Deep moist
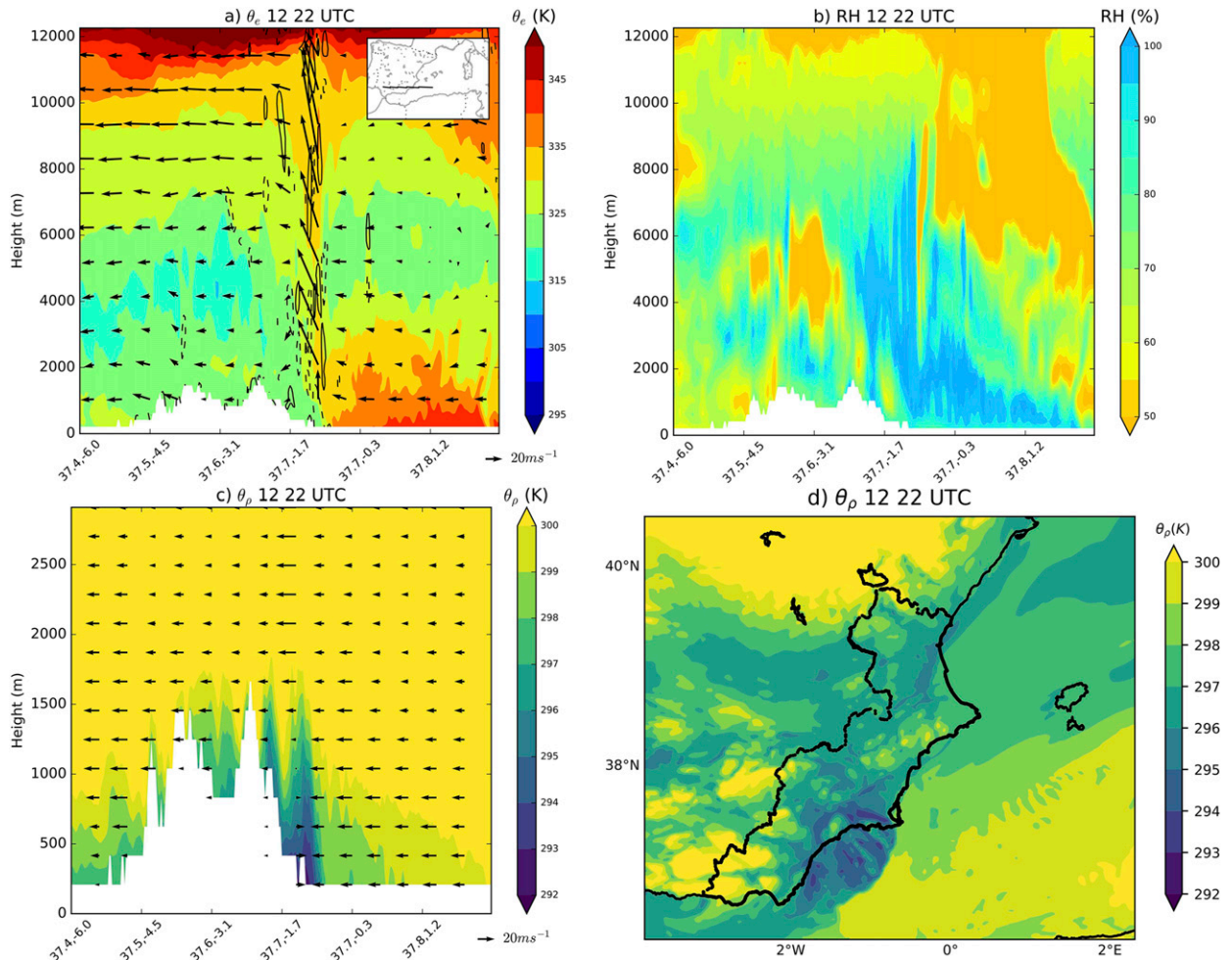
FIG. 14. Vertical cross sections at 2200 UTC 12 Sep 2019 along the segment represented in the inset of the top-left figure for (a) equivalent potential temperature (shaded), divergence/convergence (black lines), and wind speed (arrows, scale for vertical wind is 10 times horizontal scale); (b) relative humidity; (c) and density potential temperature (shaded) and horizontal wind component (arrows). The vertical scale in (c) is different from that of (a) and (b). (d) The horizontal distribution of density potential temperature on the third model level (approximately 950 hPa) around the study area.

convection developed along a boundary between a high θ_e (>335 K) air mass, which extended up to 2000 m in height and a cooler and drier air mass over land (Fig. 14a). At this stage, a definite cold outflow developed as a result of the evaporation over unsaturated areas (Figs. 14b,c). Following Tompkins (2001) and Drager and van den Heever (2017), the cold pool is identified through the density potential temperature θ_ρ:

$$\theta_\rho = \theta \frac{1 + \frac{R_v}{R_d} r_v}{1 + r_{\text{tot}}}, \tag{3}$$

where R_v and R_d stand for the gas constants of water vapor and dry air, respectively; r_v is the water vapor mixing ratio and r_{tot} denotes the total mixing ratio of water vapor and all condensate species (i.e., cloud water, rain, ice, snow, graupel, and hail). This outflow, together with the continuous moist easterly flow, contributed to the triggering of new convective cells, which

supported the MCS during the first hours of 13 September. The MCS quasi-stationarity could have been produced by the balance between the environmental flow and the cold outflow (Zhao et al. 2020). This idea is further investigated by comparing environmental wind speed with the propagation speed of the density current associated with the outflow. Following Liu and Moncrieff (2000), the density current speed C is estimated by

$$C = \text{Fr} \sqrt{gh \frac{\Delta\theta_\rho}{\overline{\theta}_\rho}}, \tag{4}$$

where Fr is the Froude number, g the acceleration of gravity, h the height of the outflow, and $\Delta\theta_\rho$ the difference between outflow and environmental θ_ρ. The density current speed C is estimated using Fr = 0.75, which is based on previous studies of density currents (e.g., Wakimoto 1982; Zhao et al. 2020), h is set to 1500 m, $\Delta\theta_\rho$ to 7 K, and $\overline{\theta}_\rho$ to 299 K (Figs. 14b,c). With these parameters,
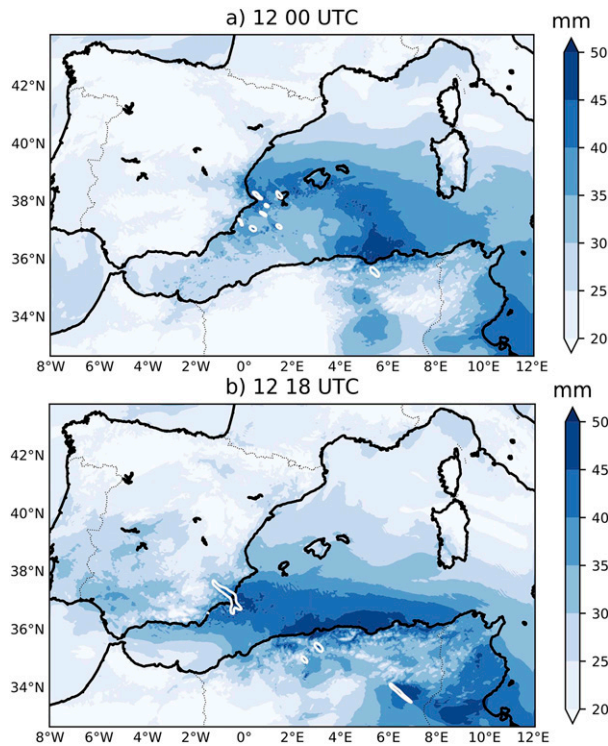
FIG. 15. Precipitable water for the control simulation at (a) 0000 and (b) 1800 UTC 12 Sep. White contours denote areas with water vapor flux convergence larger than $10 \, \mathrm{g \, m^{-2} \, s^{-1}}$.

$C \approx 14 \, \mathrm{m \, s^{-1}}$, while the environmental easterly flow was between 15 and $16 \, \mathrm{m \, s^{-1}}$. This quasi-balance resulted in the stationarity of the MCS. The subsequent veering of the easterly flow broke this quasi-balance and promoted its final northward shift.

3) MAINTENANCE OF FLASH FLOOD–PRODUCING FACTORS

Long-lasting rainfall or high precipitation rates are required for flood development (Doswell et al. 1996). The presence of high moisture contents at low levels over maritime areas throughout the HPE points to evaporation as an important contributor to its unfolding. Indeed, important latent heat fluxes (exceeding $400 \, \mathrm{W \, m^{-2}}$ in some sites) were present in the marine area affected by the northeasterly flow during phase 1. Values above $200 \, \mathrm{W \, m^{-2}}$ were also found across the western Mediterranean throughout the

TABLE 2. Relative effect of distinct physical factors on 48-h accumulated precipitation, computed as the relative difference in accumulated rainfall between perturbed and control simulations over the study area and the surrounding maritime strip.

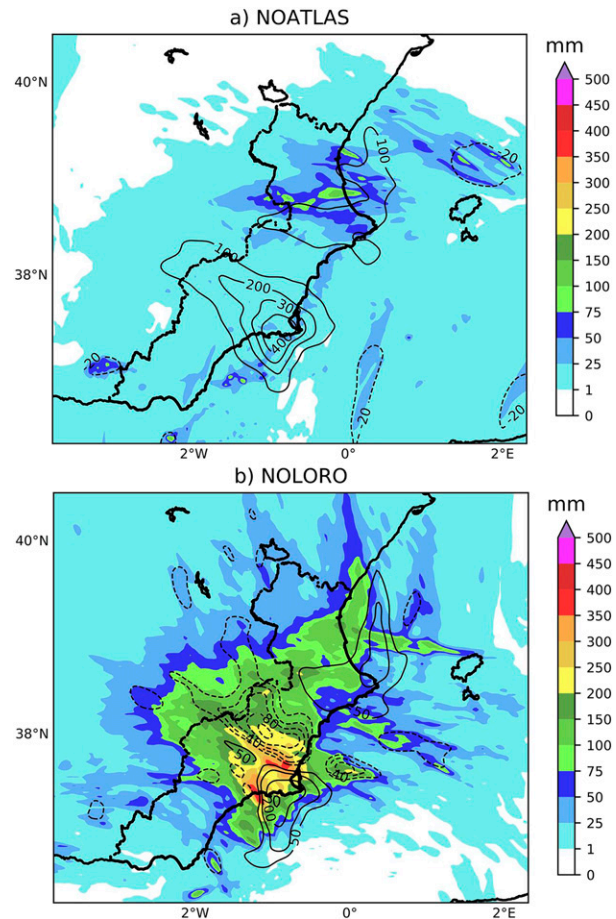| Experiment	Relative effect
NOATLAS	−75.3%
NOLORO	−12.6%
NOLHF	−56.1%
QMOD	−37.8%
SST − 1	−14.4%
SST + 1	+9.2%

FIG. 16. 48-h accumulated precipitation between 0000 UTC 12 Sep and 0000 UTC 14 Sep for the (a) NOATLAS and (b) NOLORO experiments. The difference between the accumulated precipitation in CNTL and these experiments is contoured.

entire episode (not shown). As discussed in section 2, the large-scale setting was characterized by a large area of high CAPE over the western Mediterranean, creating propitious conditions for persistent convection triggering. The favorable environment, together with the continuous moist low-level easterly flow impinging on the eastern coast of Spain resulted in the long duration of the intense precipitation on 12 September and the first hours of 13 September. Besides convection triggering, a high moisture feeding flow is required to achieve notable precipitation rates. Large values of precipitable water (PW) were detected along a tongue-shaped structure from Algeria to València during the first hours of phase 1, with values above 40 mm over the Valencian coastline (Fig. 15a). The moist air extended westward and southward after phases 1 and 2, bringing the potential for torrential precipitation into Murcia during the afternoon of 12 September (Fig. 15b).

b. Sensitivity experiments

1) OROGRAPHIC FACTORS

Orographic sensitivity experiments reveal the crucial role of the Atlas range in organizing the low level easterly flow and its
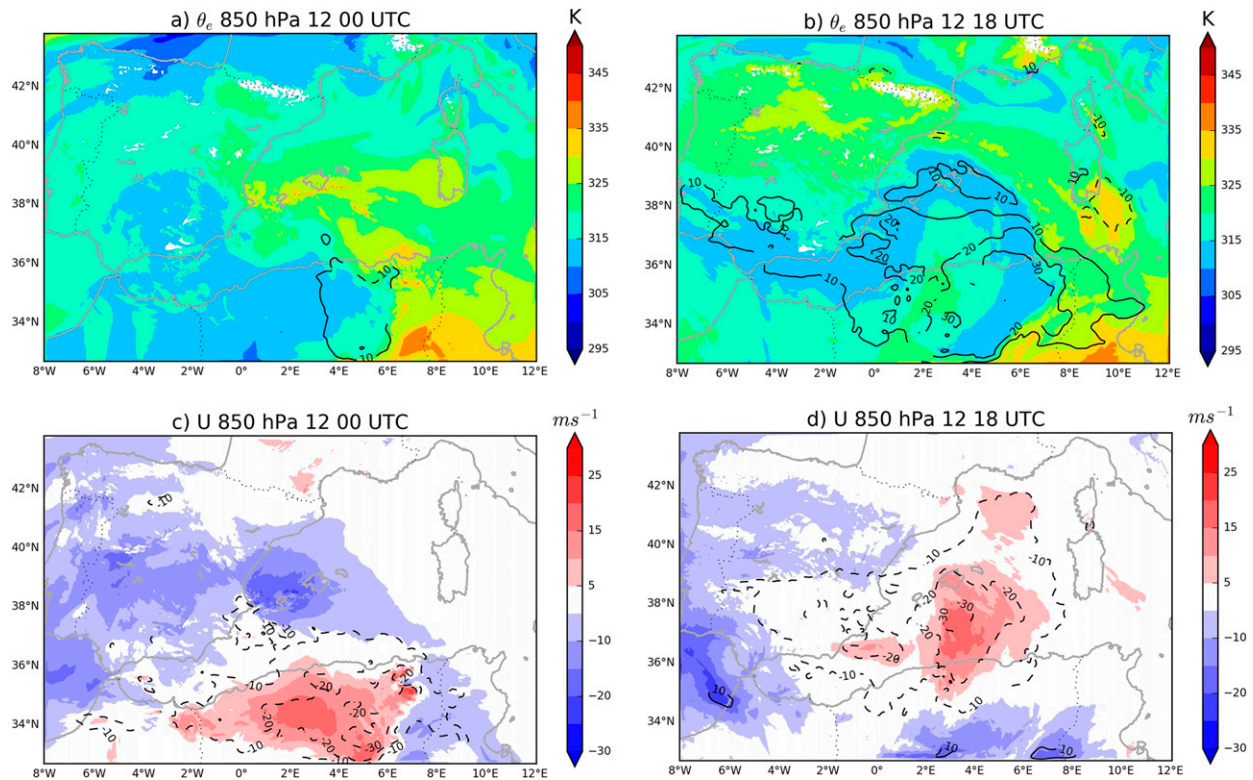
FIG. 17. (a),(b) 850-hPa equivalent potential temperature and (c),(d) *u*-wind component at (left) 0000 and (right) 1800 UTC 12 Sep for NOATLAS. Solid (dashed) contours depict a positive (negative) effect of the Atlas range on these fields.

importance in producing the observed precipitation amounts. Cumulative rainfall in NOATLAS is substantially lower than in CNTL, with a maximum accumulation barely exceeding 100 mm and a reduction of up to 75% when compared to CNTL (Table 2, Fig. 16a). This essential function of the Atlas range is in agreement with other HPEs affecting eastern Spain (Ramis et al. 1998; Homar et al. 1999). Most precipitation is produced during the period corresponding to phase 1. A moderate decrease in rainfall (~6%) is obtained in this early stage, while precipitation is negligible for longer lead times, with losses above 90% for the subsequent phases. In the absence of the Atlas, warm and moist air is not advected at low levels during phase 3 as a consequence of the suppression of the lee cyclone and the associated easterly flow (Fig. 17). As a result, instability is not reinforced, and convective activity is only marginal. Regarding the first hours of simulation, the easterly flow impinging on Cap de la Nau is still present from the ICs, and contributes to produce some precipitation. Therefore, the orographic influence identified in the NOATLAS experiment is essential for long-lasting rainfall along eastern Spain. That is, it modulates the easterly flow over the western Mediterranean, which is necessary to maintain the continuous moisture supply toward the affected area.

On the other hand, local orography impacts both precipitation accumulation and distribution at small scales (~few tens of kilometers; Fig. 16b). Deep convection is more intense in CNTL, which confirms the preeminent role of local orography

as a convection triggering and anchoring mechanism. Overall precipitation is modified when local orography is perturbed. NOLORO results corroborate the key role of local topography during phase 1, as it favors the anchoring of the linear convective system along Cap de la Nau, increasing cumulative rainfall. A similar effect is obtained over Murcia for the last phase: precipitation rate is reduced when the orography is flattened as rainfall persistence decreases, losing stationarity. Depth of the density current is slightly reduced and, consequently its speed. This explains the lower stationarity of the MCS and its westward shift with respect to the unperturbed simulation (Fig. 18). In line with other HPEs affecting the Mediterranean region (e.g., Ducrocq et al. 2008; Barthlott and Davolio 2015; Gascón et al. 2016), the central role of local orography in organizing convective activity and producing long-lasting precipitation is confirmed (Table 2). Modification of the precipitation characteristics—especially its stationarity—is of the utmost importance given the short response times to heavy rainfall of the small catchments in the study region.

2) WATER VAPOR SOURCES

The important role of evaporation from the Mediterranean Sea for the 12–13 September 2019 episode is confirmed by the NOLHF experiment. This simulation verifies its influence to supply moisture at low levels, increasing water vapor content which, in turn, increases precipitation rates. Nevertheless, it should be noted that not only a high humidity content, but also
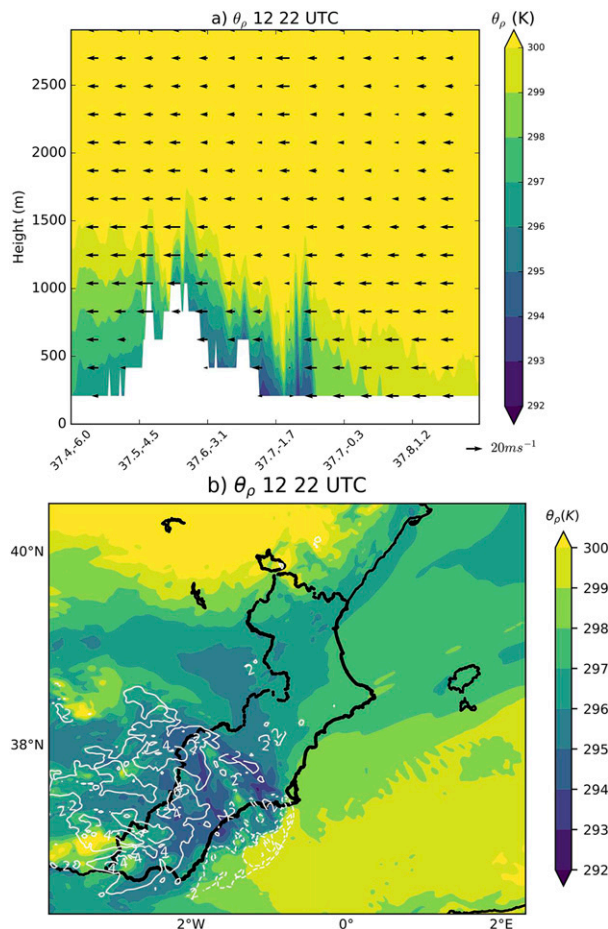
FIG. 18. (a),(b) As in Figs. 14c and 14d, but for NOLORO. White contours in (b) represent the effect of local orography on θ_ρ (i.e., $\theta_{\rho_{CNTL}} - \theta_{\rho_{NOLORO}}$).

FIG. 19. As in Fig. 15, but for NOLHF experiment. Solid (dashed) contours indicate a positive (negative) effect of latent heat flux on PW.

a large number of cloud condensation nuclei are required to produce extreme rainfall rates. An extensive reduction of total rainfall is obtained in the NOLHF experiment (Table 2). PW is considerably reduced in this experiment, especially during phase 3 (Fig. 19), and, consequently, maximum accumulations barely reach 100 mm (Fig. 20a), well below the 574 mm obtained in CNTL. Furthermore, the highest accumulations are produced during phases 1 and 2, when the effect of evaporation is limited. However, rainfall decline is more pronounced during phase 3 as a result of the accumulated moisture deficit. Thus, evaporation from the sea during the first hours of 12 September is proven essential for the development of deep convection in the last phase and to extend the duration of heavy precipitation.

Experiment QMOD confirms the critical effect of lower-troposphere moisture content on precipitation prior to the unfolding of the HPE. The thermodynamic environment during the first hours of 12 September in QMOD presents important differences with respect to CNTL. The high θ_e air mass spanning from south Sardinia to Cap de la Nau does not form, dramatically reducing convective instability over the sea. Indeed, the signature of this modification is clearly traceable at
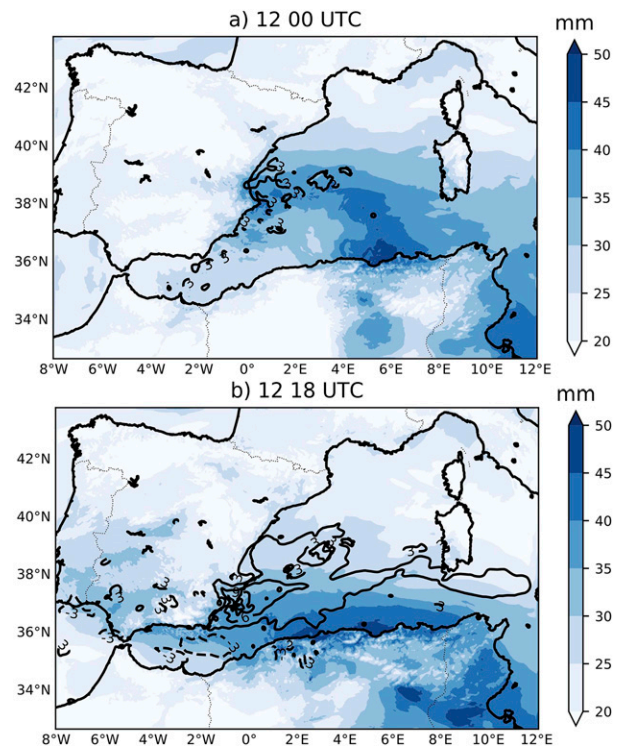
the beginning of phase 3, with a significant reduction of θ_e over Murcia, produced by the southeasterly advection of the low θ_e air mass. Hence, the simulated precipitation during phase 1 in QMOD is reduced by up to 75% (Table 2, Fig. 20b). Therefore, the precipitation occurring during the first hours of 12 September can be attributed to moisture advection from the Tyrrhenian Sea. This reduction extends to the subsequent phases rendering a considerable decline in cumulative rainfall (Table 2). Specific humidity perturbation yields an additional modification of total rainfall amount as its maximum is displaced southward because the most favorable area for convective development during phases 1 and 2 is also shifted accordingly. This effect combined with the decrease in moisture availability—which affects southern València and Murcia during phase 3—causes notable variations in the accumulated rainfall pattern. The considerable sensitivity of both the location and intensity of extreme precipitation to evaporative fluxes and moisture highlight a critical challenge for the correct numerical forecasting of HPEs resulting in flash floods over Mediterranean Spain. The scarcity of observations over maritime areas generates a substantial uncertainty in the specification of these factors. Indeed, Part II of this study is devoted to tackling these uncertainties and investigating their propagation in runoff simulations.

3) SEA SURFACE TEMPERATURE

The essential role of latent heat fluxes on 12 September in providing enough moisture at low levels suggests that SST is also a critical predictability controller. SST $\pm$ 1 experiments

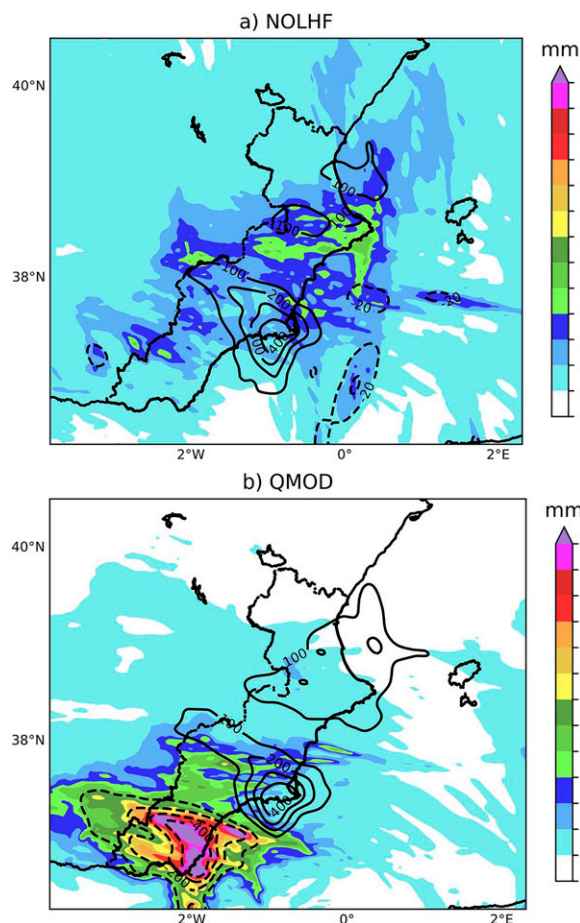FIG. 20. As in Fig. 16, but for (a) NOLHF and (b) QMOD experiments.

FIG. 21. As in Fig. 16, but for (a) SST − 1 and (b) SST + 1 experiments.

aim to quantify this sensitivity. The change of 1°C produces a modification of air–sea heat fluxes across the domain. This change renders a slight variation of θ_e over the sea between North Africa and the southeastern Iberian Peninsula. This effect is attributable to a modification in the latent heat flux, which results in an alteration of accumulated precipitation throughout the entire episode (Table 2, Fig. 21). Areal average precipitation varies linearly with SST. However, changes in maximum rainfall are more intense when the temperature is increased. The uniform decrease in SST leads to a 21% reduction in 48-h maximum accumulated precipitation. By contrast, the maximum in the SST + 1 experiment is 45% greater than in CNTL.

An additional interesting result is the significant redistribution of the precipitation pattern. The location of the maximum rainfall during phase 3 is highly sensitive to the SST. The orographic perturbation generated by the Atlas range redirected the flow toward the eastern Iberian Peninsula, producing an area of high moisture convergence. The effect of the heating (cooling) of sea surface results in an intensification (weakening) of the cyclonic circulation, which modulates the orographically perturbed flow. The area of moisture convergence is moved northward (southward) when SST is increased (reduced), yielding differences in the area of highest rainfall of
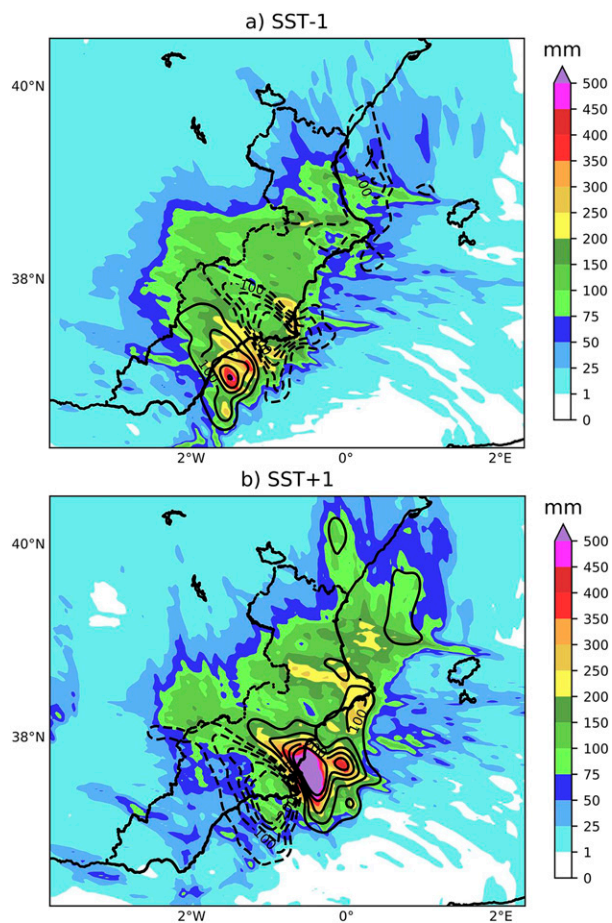
approximately 60 km per SST degree variation (Figs. 21 and 22). This alteration in precipitation location is consistent with other HPEs in the region (e.g., Senatore et al. 2014; Demirtaş 2016; Ivatek-Šahdan et al. 2018). In these episodes, changes in SST produced slight variations in the flow which significantly affected total rainfall, while higher SST favored maritime convective activity, reducing inland precipitation.

The impact of SST in modifying not only precipitation intensity, but also its location has critical implications for the predictability of the 12–13 September 2019 episode. Uncertainties in the SST can result in QPFs misplacing heavy rainfall over small-to-medium basins, impacting subsequent quantitative discharge forecasts and flash flood warnings. This is a crucial issue when forecasting HPEs as current satellite measurements have an approximate accuracy of 0.5°C, while in situ observations from ships have uncertainties of 1.0°–1.5°C and buoy measurements present errors between 0.1° and 0.7°C (O'Carroll et al. 2019, and references therein). This range of SST uncertainties can produce substantial displacements in rainfall distribution according to these experiments. As an illustrative example, errors in the SST analyses by the Copernicus Marine Environment Monitoring Service (CMEMS) for 11, 12, and 13 September are shown in Fig. 23. These fields reveal inaccuracies between 0.5° and 1°C over large
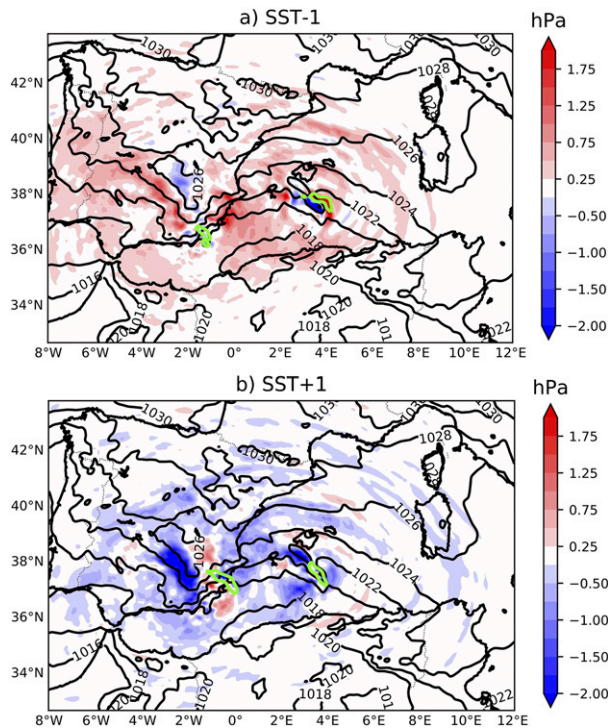
FIG. 22. Sea level pressure difference between simulations with perturbed SST and CNTL (contoured colors; hPa) for (a) SST − 1 and (b) SST + 1. Reference sea level pressure from CNTL is depicted in solid black contours (hPa), and areas with water vapor flux convergence greater than $10 \, \mathrm{g \, m^{-2} \, s^{-1}}$ are contoured in green.

areas of the western Mediterranean, which would lead to substantial differences in 48-h precipitation location and intensity. Furthermore, the SST is kept constant throughout the simulations, adding further imprecisions that are not usually considered in real-time weather forecasting. Indeed, divergences of the order of 1°C are found between the CMEMS and the ECMWF analyses used in the simulations (Fig. 23).

5. Conclusions

An analysis of the 12–13 September 2019 widespread heavy precipitation episode in eastern Spain was conducted using observational data sources and numerical simulations. The high resolution required to produce accurate quantitative precipitation forecasts severely restricts the predictability horizon of convection and subsequent flash flooding. This fact combined with the long time span of this episode makes precise QPF extremely challenging. However, the presence of many small-to-medium size catchments requires accurate QPFs in order to obtain valuable quantitative discharge forecasts. The findings of the first part of this study contribute to offer a better understanding of the mesoscale and local-scale mechanisms related to the initiation and evolution of flash flood inducing convective systems.

The synoptic situation was characterized by a nearly stationary upper-level cold cutoff low located over North Africa during 12 and 13 September, combined with an easterly flow

over the western Mediterranean, advecting warm and moist air toward the València and Murcia regions. The high-resolution numerical simulation unveiled that the thermodynamical environment was defined by an area of intense θ_e and convective instability over the sea during the first hours of 12 September. This setting established the most favorable areas for convective development over Cap de la Nau during the first hours and Vega Baja afterward. During the last hours of 12 September, an area of intense convective instability was identified offshore Murcia. This acute instability together with a strong moisture convergence, yielded the appropriate environment to develop sustained deep moist convection.

The episode was divided into three phases based on an analysis of the different convective systems: (i) a quasi-stationary thin convective band over Cap de la Nau at 0000–0600 UTC 12 September, (ii) a linear structure upon Vega Baja at 0600–1200 UTC 12 September, and (iii) a mesoscale convective system initially affecting Murcia and subsequently evolving northward. Additional convective bands impacted western Almería during this phase, which extended from 1800 UTC 12 September to 1200 UTC 13 September. A precise representation of the first and second phases is especially critical, given the limited spatial extent of the precipitation and the strong influence of local orography.

The control numerical simulation reproduced the observed synoptic and mesoscale environment and the main features of the radar-derived precipitation fields, including the warm and moist easterly flow at low levels which contributed to convectively destabilize the environment over València and Murcia. Furthermore, the control simulation together with the observational diagnostic suggested the relevance of local orography to anchor convective systems, thus generating persistent precipitation conducive to widespread flash flooding. Maritime evaporation was identified as a preeminent moisture source which increased precipitable water availability and rainfall rate. Furthermore, a quasi-balance between the environmental easterly flow and the outflow from the MCS contributed to its stationarity.

Experiments with modified orography revealed the crucial role of the Atlas range in organizing the easterly flow necessary to transport moisture to the eastern coast of Spain and to sustain long-lasting high precipitation rates. Indeed, more than 75% of the total precipitation was attributable to this factor. Moreover, local orography produced orographic anchoring altering the precipitation pattern. This factor was found to be decisive in the large rainfall amounts over Cap de la Nau and for MCS stationarity in Murcia during phases 1 and 3, respectively.

Maritime evaporation also had a considerable impact on precipitation throughout the entire episode. Its influence was more intense in the last phase, revealing that evaporation during the first hours of 12 September was crucial to generating the subsequent high moisture availability for the next hours. Furthermore, the tropospheric moisture already present over the Tyrrhenian Sea was essential to produce a high moisture and convective instability area over the sea during the first hours of 12 September, favoring the development of convective activity in Cap de la Nau and Vega Baja. Modification of
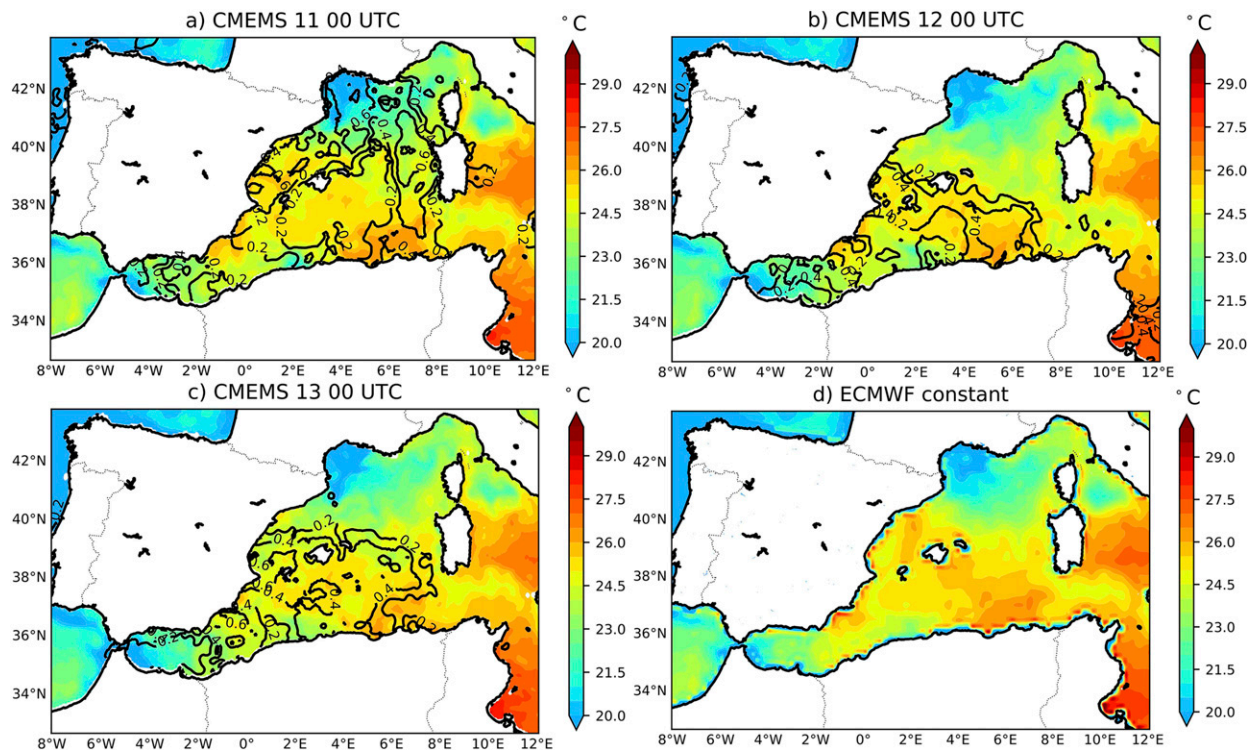
FIG. 23. Comparison of the SST (contoured colors; °C) of CMEM analyses for 0000 UTC (a) 11, (b) 12, and (c) 13 Sep 2019. (d) The SST analysis obtained by ECMWF initialization and used in the control simulation. CMEMS SST analysis errors are represented as solid contours in (a)–(c).

stability and moisture content implies a southward shift of the precipitation during the last phase. This additional effect involves a critical issue for QPFs since a wide diversity of risk scenarios arose under different moisture conditions. This fact reveals the need for having accurate three-dimensional humidity data over maritime areas in order to improve the quality of the analyses and thus the initial and boundary conditions for numerical weather prediction.

In addition, a remarkable sensitivity in the location and intensity of rainfall patterns to the SST was found. Heating or cooling of the sea surface produced changes in latent heat flux which, in turn, modified moisture availability and precipitation rate. Concurrently, sea level pressure and the associated cyclonic circulation were also modified, strongly affecting moisture convergence area during phase 3. This resulted in a shifting of the maximum precipitation accumulation of approximately 60 km per SST degree variation. This acute sensitivity raises a crucial concern for flood forecasting purposes: typical errors in current SST analyses can easily produce noticeable changes in the distribution and intensity of extreme precipitation, severely hampering the short-range forecasting of HPEs. Hence, very precise SST analyses are required in order to accurately predict the localization and intensity of convective systems. Predictability could be improved by adopting coupled atmosphere–ocean models to update SST throughout the forecast, thereby reducing the associated errors (e.g., Strajnar et al. 2019).

These sensitivity experiments highlight the need for accurate initial conditions in order to reproduce socially sensitive aspects in extreme rainfall such as timing, intensity, and location. These features are found to be extremely sensitive to both preexisting tropospheric moisture content and sea surface temperature. Improvement in observations and data assimilation techniques emerges as a crucial issue so as to reduce associated uncertainties, particularly over maritime regions due to the limited number of in situ observations. Additionally, advanced ensemble generation strategies should comprehensively sample initial, boundary and model formulation uncertainties to improve quantitative precipitation forecasts of HPEs so as to prevent human and material losses. In this sense, the second part of this study tackles these predictability issues by means of cutting-edge ensemble generation techniques.

reviewers are deeply acknowledged for their valuable comments that helped to improve the quality of this manuscript.

Data availability statement. Access to ECMWF, AEMET, and data from the hydrological confederations are subject to the terms and conditions applied by these agencies. Experimental data can be provided by the authors under request.

REFERENCES

Amponsah, W., and Coauthors, 2018: Integrated high-resolution dataset of high-intensity European and Mediterranean flash floods. *Earth Syst. Sci. Data*, **10**, 1783–1794, https://doi.org/10.5194/essd-10-1783-2018.

Barthlott, C., and S. Davolio, 2015: Mechanisms initiating heavy precipitation over Italy during HyMeX Special Observation Period 1: A numerical case study using two mesoscale models. *Quart. J. Roy. Meteor. Soc.*, **142**, 238–258, https://doi.org/10.1002/qj.2630.

Borga, M., P. Boscolo, F. Zanon, and M. Sangati, 2007: Hydrometeorological analysis of the 29 August 2003 flash flood in the eastern Italian Alps. *J. Hydrometeor.*, **8**, 1049–1067, https://doi.org/10.1175/JHM593.1.

Bouilloud, L., B. Delrieu, B. Boudevillain, M. Borga, and F. Zanon, 2009: Radar rainfall estimation for the post-event analysis of a Slovenian flash-flood case: Application of the Mountain Reference Technique at C-band frequency. *Hydrol. Earth Syst. Sci.*, **13**, 1349–1360, https://doi.org/10.5194/hess-13-1349-2009.

Bresson, E., V. Ducrocq, O. Nuissier, D. Ricard, and C. de Saint-Aubin, 2012: Idealized numerical simulations of quasi-stationary convective systems over the northwestern Mediterranean complex terrain. *Quart. J. Roy. Meteor. Soc.*, **138**, 1751–1763, https://doi.org/10.1002/qj.1911.

Buzzi, A., N. Tartaglione, and P. Malguzzi, 1998: Numerical simulations of the 1994 piedmont flood: Role of orography and moist processes. *Mon. Wea. Rev.*, **126**, 2369–2383, https://doi.org/10.1175/1520-0493(1998)126<2369:NSOTPF>2.0.CO;2.

——, S. Davolio, P. Malguzzi, O. Drofa, and D. Mastrangelo, 2014: Heavy rainfall episodes over Liguria in autumn 2011: Numerical forecasting experiments. *Nat. Hazards Earth Syst. Sci.*, **14**, 1325–1340, https://doi.org/10.5194/nhess-14-1325-2014.

CCS, 2019: Cuarta nota informativa del consorcio de compensación de seguros sobre las inundaciones producidas entre los días 11 y 15 de septiembre en el sureste principalmente. Consorcio de Compensación de Seguros, 4 pp., https://www.consorseguros.es/web/noticias/-/asset_publisher/ya2OdYGgbjgX/content/cuarta-nota-informativa-del-consorcio-de-compensacion-de-seguros-sobre-las-inundaciones-producidas-entre-los-dias-11-y-15-de-septiembre-en-el-sureste-.

Cole, S., and R. Moore, 2008: Hydrological modelling using rain-gauge- and radar-based estimators of areal rainfall. *J. Hydrol.*, **358**, 159–181, https://doi.org/10.1016/j.jhydrol.2008.05.025.

Cosma, S., E. Richard, and F. Miniscloux, 2002: The role of small-scale orographic features in the spatial distribution of precipitation. *Quart. J. Roy. Meteor. Soc.*, **128**, 75–92, https://doi.org/10.1256/00359000260498798.

Davolio, S., A. Buzzi, and P. Malguzzi, 2009: Orographic triggering of long lived convection in three dimensions. *Meteor. Atmos. Phys.*, **103**, 35–44, https://doi.org/10.1007/s00703-008-0332-5.

Delrieu, G., and Coauthors, 2005: The catastrophic flash-flood event of 8–9 September 2002 in the Gard Region, France: A first case study for the Cévennes–Vivarais Mediterranean

Hydrometeorological Observatory. *J. Hydrometeor.*, **6**, 34–52, https://doi.org/10.1175/JHM-400.1.

Demirtaş, M., 2016: The October 2011 devastating flash flood event of Antalya: Triggering mechanisms and quantitative precipitation forecasting. *Quart. J. Roy. Meteor. Soc.*, **142**, 2336–2346, https://doi.org/10.1002/qj.2827.

Doswell, C., H. Brooks, and R. Maddox, 1996: Flash flood forecasting: An ingredients-based methodology. *Wea. Forecasting*, **11**, 560–581, https://doi.org/10.1175/1520-0434(1996)011<0560:FFFAIB>2.0.CO;2.

——, C. Ramis, R. Romero, and S. Alonso, 1998: A diagnostic study of three heavy precipitation episodes in the western Mediterranean region. *Wea. Forecasting*, **13**, 102–124, https://doi.org/10.1175/1520-0434(1998)013<0102:ADSOTH>2.0.CO;2.

Dougherty, E., and K. Rasmussen, 2019: Climatology of flood-producing storms and their associated rainfall characteristics in the United States. *Mon. Wea. Rev.*, **147**, 3861–3877, https://doi.org/10.1175/MWR-D-19-0020.1.

Drager, A., and S. van den Heever, 2017: Characterizing convective cold pools. *J. Adv. Model. Earth Syst.*, **9**, 1091–1115, https://doi.org/10.1002/2016MS000788.

Drobinski, P., and Coauthors, 2014: HyMeX: A 10-year multidisciplinary program on the Mediterranean water cycle. *Bull. Amer. Meteor. Soc.*, **95**, 1063–1082, https://doi.org/10.1175/BAMS-D-12-00242.1.

Ducrocq, V., O. Nuissier, D. Ricard, C. Lebeaupin, and T. Thouvenin, 2008: A numerical study of three catastrophic precipitating events over southern France. II: Mesoscale triggering and stationarity factors. *Quart. J. Roy. Meteor. Soc.*, **134**, 131–145, https://doi.org/10.1002/qj.199.

Duffourg, F., and V. Ducrocq, 2011: Origin of the moisture feeding the heavy precipitating systems over southeastern France. *Nat. Hazards Earth Syst. Sci.*, **11**, 1163–1178, https://doi.org/10.5194/nhess-11-1163-2011.

Fiori, E., A. Comellas, L. Molini, N. Rebora, F. Siccardi, D. J. Gochis, S. Tanelli, and A. Parodia, 2014: Analysis and hindcast simulations of an extreme rainfall event in the Mediterranean area: The Genoa 2011 case. *Atmos. Res.*, **138**, 13–29, https://doi.org/10.1016/j.atmosres.2013.10.007.

Fulton, R., J. Breidenbach, D. Seo, D. Miller, and T. O'Bannon, 1998: The WSR-88D rainfall algorithm. *Wea. Forecasting*, **13**, 377–395, https://doi.org/10.1175/1520-0434(1998)013<0377:TWRA>2.0.CO;2.

García-Herrera, R., D. Barropedro, E. Hernández, D. Paredes, J. F. Correoso, and L. Prieto, 2005: The 2001 mesoscale convective systems over Iberia and the Balearic Islands. *Meteor. Atmos. Phys.*, **90**, 225–243, https://doi.org/10.1007/s00703-005-0114-2.

Gascón, E., S. Laviola, A. Merino, and M. Miglietta, 2016: Analysis of a localized flash-flood event over the central Mediterranean. *Atmos. Res.*, **182**, 256–268, https://doi.org/10.1016/j.atmosres.2016.08.007.

Gochis, D., and Coauthors, 2015: The great Colorado flood of September 2013. *Bull. Amer. Meteor. Soc.*, **96**, 1461–1487, https://doi.org/10.1175/BAMS-D-13-00241.1.

Han, J., and S. Hong, 2018: Precipitation forecast experiments using the Weather Research and Forecasting (WRF) Model at gray-zone resolutions. *Wea. Forecasting*, **33**, 1605–1616, https://doi.org/10.1175/WAF-D-18-0026.1.

Hermoso, A., V. Homar, S. Greybush, and D. Stensrud, 2020: Tailored ensemble prediction systems: Application of seamless scale bred vectors. *J. Meteor. Soc. Japan*, **98**, 1029–1050, https://doi.org/10.2151/jmsj.2020-053.

Hohenegger, C., and C. Schär, 2007: Predictability and error growth dynamics in cloud-resolving models. *J. Atmos. Sci.*, **64**, 4467–4478, https://doi.org/10.1175/2007JAS2143.1.

Homar, V., C. Ramis, R. Romero, S. Alonso, J. García Moya, and M. Alarcón, 1999: A case of convection development over the western Mediterranean Sea: A study through numerical simulations. *Meteor. Atmos. Phys.*, **71**, 169–188, https://doi.org/10.1007/s007030050054.

——, ——, and S. Alonso, 2002: A deep cyclone of African origin over the western Mediterranean: Diagnosis and numerical simulation. *Ann. Geophys.*, **20**, 93–106, https://doi.org/10.5194/angeo-20-93-2002.

——, R. Gayà, R. Romero, C. Ramis, and S. Alonso, 2003: Tornadoes over complex terrain: An analysis of the 28th August 1999 tornadic event in eastern Spain. *Atmos. Res.*, **67–68**, 301–317, https://doi.org/10.1016/S0169-8095(03)00064-4.

Hunter, S., 1996: WSR-88D radar rainfall estimation: Capabilities, limitations and potential improvements. *Natl. Wea. Dig.*, **20**, 26–36.

Iacono, M., J. Delamere, E. Mlawer, M. Shephard, S. Clough, and W. Collins, 2008: Radiative forcing by long-lived greenhouse gases: Calculations with the AER radiative transfer models. *J. Geophys. Res.*, **113**, D13103, https://doi.org/10.1029/2008JD009944.

Ivatek-Šahdan, S., A. Stanešić, M. Tudor, I. Odak Plenković, and I. Janeković, 2018: Impact of SST on heavy rainfall events on eastern Adriatic during SOP1 of HyMeX. *Atmos. Res.*, **200**, 36–59, https://doi.org/10.1016/j.atmosres.2017.09.019.

Kain, J., and Coauthors, 2008: Some practical considerations regarding horizontal resolution in the first generation of operational convection-allowing NWP. *Wea. Forecasting*, **23**, 931–952, https://doi.org/10.1175/WAF2007106.1.

Kirshbaum, D., G. Bryan, R. Rotunno, and D. Durran, 2007: The triggering of orographic rainbands by small-scale topography. *J. Atmos. Sci.*, **64**, 1530–1549, https://doi.org/10.1175/JAS3924.1.

Lebeaupin, C., V. Ducrocq, and H. Giordani, 2006: Sensitivity of torrential rain events to the sea surface temperature based on high-resolution numerical forecasts. *J. Geophys. Res.*, **111**, D12110, https://doi.org/10.1029/2005JD006541.

Liu, C., and M. Moncrieff, 2000: Simulated density currents in idealized stratified environments. *Mon. Wea. Rev.*, **128**, 1420–1437, https://doi.org/10.1175/1520-0493(2000)128<1420:SDCIIS>2.0.CO;2.

Llasat, M. C., and M. Puigcerver, 1994: Meteorological factors associated with floods in the north-eastern part of the Iberian Peninsula. *Nat. Hazards*, **9**, 81–93, https://doi.org/10.1007/BF00662592.

——, M. Llasat-Botija, A. Rodríguez, and S. Lindbergh, 2010: Flash floods in Catalonia: A recurrent situation. *Adv. Geosci.*, **26**, 105–111, https://doi.org/10.5194/adgeo-26-105-2010.

Mansell, E., C. Ziegler, and E. Bruning, 2010: Simulated electrification of a small thunderstorm with two-moment bulk microphysics. *J. Atmos. Sci.*, **67**, 171–194, https://doi.org/10.1175/2009JAS2965.1.

Marchi, L., M. Borga, E. Preciso, and E. Gaume, 2010: Characterisation of selected extreme flash floods in Europe and implications for flood risk management. *J. Hydrol.*, **394**, 118–133, https://doi.org/10.1016/j.jhydrol.2010.07.017.

Martín, A., R. Romero, V. Homar, A. De Luque, S. Alonso, T. Rigo, and M. C. Llasat, 2007: Sensitivities of a flash flood event over Catalonia: A numerical analysis. *Mon. Wea. Rev.*, **135**, 651–669, https://doi.org/10.1175/MWR3316.1.

Martínez, C., J. Campins, A. Jansà, and A. Genovés, 2008: Heavy rain events in the western Mediterranean: An atmospheric pattern classification. *Adv. Sci. Res.*, **2**, 61–64, https://doi.org/10.5194/asr-2-61-2008.

Michaelides, S., and Coauthors, 2018: Reviews and perspectives of high impact atmospheric processes in the Mediterranean. *Atmos. Res.*, **208**, 4–44, https://doi.org/10.1016/j.atmosres.2017.11.022.

Mogensen, K., M. Alonso Balmaseda, and A. Weaver, 2012: The NEMOVAR ocean data assimilation system as implemented in the ECMWF ocean analysis for System 4. ECMWF Tech. Memo. 668, 59 pp., https://www.ecmwf.int/en/elibrary/11174-nemovar-ocean-data-assimilation-system-implemented-ecmwf-ocean-analysis-system-4.

Nakanishi, M., and H. Niino, 2006: An improved Mellor-Yamada level-3 model: Its numerical stability and application to a regional prediction of advection fog. *Bound.-Layer Meteor.*, **119**, 397–407, https://doi.org/10.1007/s10546-005-9030-8.

Nuissier, O., D. Ducrocq, D. Ricard, C. Lebeaupin, and S. Anquetin, 2008: A numerical study of three catastrophic precipitating events over southern France. I: Numerical framework and synoptic ingredients. *Quart. J. Roy. Meteor. Soc.*, **134**, 111–130, https://doi.org/10.1002/qj.200.

O'Carroll, A., and Coauthors, 2019: Observational needs of sea surface temperature. *Front. Mar. Sci.*, **6**, 420, https://doi.org/10.3389/fmars.2019.00420.

Pastor, F., I. Gómez, and M. Estrela, 2010: Numerical study of the October 2007 flash flood in the Valencia region (eastern Spain): The role of orography. *Nat. Hazards Earth Syst. Sci.*, **10**, 1331–1345, https://doi.org/10.5194/nhess-10-1331-2010.

——, J. Valiente, and M. Estrela, 2015: Sea surface temperature and torrential rains in the Valencia region: Modelling the role of recharge areas. *Nat. Hazards Earth Syst. Sci.*, **15**, 1677–1693, https://doi.org/10.5194/nhess-15-1677-2015.

Pellarin, T., G. Delrieu, G. Saulnier, H. Andrieu, B. Vignal, and J. Creutin, 2002: Hydrologic visibility of weather radar systems operating in mountainous regions: Case study for the Ardèche Catchment (France). *J. Hydrometeor.*, **3**, 539–555, https://doi.org/10.1175/1525-7541(2002)003<0539:HVOWRS>2.0.CO;2.

Rainaud, R., C. Brossier, V. Ducrocq, and H. Giordani, 2017: High-resolution air-sea coupling impact on two heavy precipitation events in the western Mediterranean. *Quart. J. Roy. Meteor. Soc.*, **143**, 2448–2462, https://doi.org/10.1002/qj.3098.

Ramis, C., M. C. Llasat, A. Genovés, and A. Jansà, 1994: The October-1987 floods in Catalonia: Synoptic and mesoscale mechanisms. *Meteor. Appl.*, **1**, 337–350, https://doi.org/10.1002/met.5060010404.

——, R. Romero, V. Homar, S. Alonso, and M. Alarcón, 1998: Diagnosis and numerical simulation of a torrential precipitation event in Catalonia (Spain). *Meteor. Atmos. Phys.*, **69**, 1–21, https://doi.org/10.1007/BF01025180.

Romero, R., G. Sumner, C. Ramis, and A. Genovés, 1999: A classification of the atmospheric circulation patterns producing significant daily rainfall in the Spanish Mediterranean area. *Int. J. Climatol.*, **19**, 765–785, https://doi.org/10.1002/(SICI)1097-0088(19990615)19:7<765::AID-JOC388>3.0.CO;2-T.

Senatore, A., G. Mendicino, H. Knoche, and H. Kunstmann, 2014: Sensitivity of modeled precipitation to sea surface temperature in regions with complex topography and coastlines: A case study for the Mediterranean. *J. Hydrometeor.*, **15**, 2370–2396, https://doi.org/10.1175/JHM-D-13-089.1.

Sénési, S., P. Bougeault, J. Chèze, P. Cosentino, and R. Thepenier, 1996: The Vaison-La-Romaine flash flood: Mesoscale analysis

and predictability issues. *Wea. Forecasting*, **11**, 417–442, https://doi.org/10.1175/1520-0434(1996)011<0417:TVLRFF>2.0.CO;2.

Skamarock, W. C., and Coauthors, 2008: A description of the Advanced Research WRF version 3. NCAR Tech. Note NCAR/TN-475+STR, 113 pp., https://doi.org/10.5065/D6DZ069T.

Smirnova, T., J. Brown, S. Benjamin, and J. Kenyon, 2016: Modifications to the Rapid Update Cycle land surface model (RUC LSM) available in the weather research and forecasting (WRF) model. *Mon. Wea. Rev.*, **144**, 1851–1865, https://doi.org/10.1175/MWR-D-15-0198.1.

Stark, J., M. Donlon, M. Martin, and M. McCulloch, 2007: OSTIA: An operational, high resolution, real time, global sea surface temperature analysis system. *OCEANS 2007 Europe*, Aberdeen, United Kingdom, IEEE, 1–4, https://doi.org/10.1109/OCEANSE.2007.4302251.

Stocchi, P., and S. Davolio, 2017: Intense air-sea exchanges and heavy orographic precipitation over Italy: The role of Adriatic sea surface temperature uncertainty. *Atmos. Res.*, **196**, 62–82, https://doi.org/10.1016/j.atmosres.2017.06.004.

Strajnar, B., J. Cedilnik, A. Fettich, M. Ličer, N. Pristov, P. Smerkol, and J. Jerman, 2019: Impact of two-way coupling and sea-surface temperature on precipitation forecasts in regional atmosphere and ocean models. *Quart. J. Roy. Meteor. Soc.*, **145**, 228–242, https://doi.org/10.1002/qj.3425.

Sun, J., S. B. Trier, Q. Xiao, M. L. Weisman, H. Wang, Z. Ying, M. Xu, and Y. Zhang, 2012: Sensitivity of 0–12-h warm-season precipitation forecasts over the central United States to model initialization. *Wea. Forecasting*, **27**, 832–855, https://doi.org/10.1175/WAF-D-11-00075.1.

Tompkins, A., 2001: Organization of tropical convection in low vertical wind shears: The role of cold pools. *J. Atmos. Sci.*, **58**, 1650–1672, https://doi.org/10.1175/1520-0469(2001)058<1650:OOTCIL>2.0.CO;2.

Turato, B., O. Reale, and F. Siccardi, 2004: Water vapor sources of the October 2000 Piedmont flood. *J. Hydrometeor.*, **5**, 693–712, https://doi.org/10.1175/1525-7541(2004)005<0693:WVSOTO>2.0.CO;2.

Wakimoto, R., 1982: The life cycle of thunderstorm gust fronts as viewed with Doppler radar and rawinsonde data. *Mon. Wea. Rev.*, **110**, 1060–1082, https://doi.org/10.1175/1520-0493(1982)110<1060:TLCOTG>2.0.CO;2.

Weisman, M., C. Davis, W. Wang, K. Manning, and J. Klemp, 2008: Experiences with 0–36-h explicit convective forecasts with the WRF-ARW model. *Wea. Forecasting*, **23**, 407–437, https://doi.org/10.1175/2007WAF2007005.1.

Zhang, Y., F. Zhang, D. Stensrud, and Z. Meng, 2015: Practical predictability of the 20 May 2013 tornadic thunderstorm event in Oklahoma: Sensitivity to synoptic timing and topographical influence. *Mon. Wea. Rev.*, **143**, 2973–2997, https://doi.org/10.1175/MWR-D-14-00394.1.

——, ——, ——, and ——, 2016: Intrinsic predictability of the 20 May 2013 tornadic thunderstorm event in Oklahoma at storm scales. *Mon. Wea. Rev.*, **144**, 1273–1298, https://doi.org/10.1175/MWR-D-15-0105.1.

Zhao, Y., C. Liu, Y. Wang, and M. Moncrieff, 2020: Quasi-stationary extreme rain produced by mesoscale convective system on the Mei-Yu front. *Meteor. Atmos. Phys.*, **132**, 721–742, https://doi.org/10.1007/s00703-019-00717-1.